

Progressive Band Subset Fusion for Hyperspectral Anomaly Detection

Fang Li^{ID}, Meiping Song, Chunyan Yu, *Member, IEEE*, Yulei Wang^{ID}, and Chein-I Chang^{ID}, *Life Fellow, IEEE*

Abstract—This article presents a new approach, called progressive band subset fusion (PBSF) for hyperspectral anomaly detection. Unlike band selection (BS) which selects bands according to band prioritization or band search strategies, PBSF fuses band subsets progressively during data collection processing. It is completely opposite to BS that must be done after data are acquired and then select bands by removing spectral redundancy as post-data processing. To accomplish PBSF, two versions of PBSF are derived: PBSF of the multiple-band subset (PBSF-MBS) and PBSF of uniform BS (PBSF-UBS). In particular, the fusion process takes place in an anomaly detector from a real-time processing perspective. Three approaches are developed to realize PBSF of two-band subsets simultaneously: PBSF-band sequential (PBSF-BSQ), PBSF-RT, and PBSF-zigzag. Extensive experiments demonstrate that PBSF has advantages over BS in many ways.

Index Terms—Anomaly detection (AD), band fusion (BF), progressive band subset fusion (PBSF).

NOMENCLATURE

AD	Anomaly detection.
BF	Band fusion.
BP	Band prioritization.
BS	Band selection.
BSQ	Band sequential.
BSS	Band subset selection.
CEM-AD	CEM anomaly detector.
HFC	Harsanyi–Farrand–Chang.
MBS	Multiple-band subset.
PBSF	Progressive band subset fusion.
PBSF-BSQ	PBSF performed by band sequential.
PBSF-MBS	PBSF of multiple-band subsets.
PBSF-RT	PBSF performed by real time.

Manuscript received 22 November 2021; revised 16 May 2022; accepted 20 June 2022. Date of publication 27 June 2022; date of current version 12 July 2022. The work of Fang Li was supported by the Cultivation Program for the Excellent Doctoral Dissertation of Dalian Maritime University under Grant 2022YBPY006. The work of Meiping Song was supported by the National Nature Science Foundation of China under Grant 61971082 and Grant 61890964. (*Corresponding author: Meiping Song*.)

Fang Li, Meiping Song, Chunyan Yu, and Yulei Wang are with the Center for Hyperspectral Imaging in Remote Sensing (CHIRS), Information and Technology College, Dalian Maritime University, Dalian 116026, China (e-mail: lifang0105@qq.com; smping@163.com; 36202986@qq.com; wangyulei@dlmu.edu.cn).

Chein-I Chang is with the Remote Sensing Signal and Image Processing Laboratory, Department of Computer Science and Electrical Engineering, University of Maryland at Baltimore County, Baltimore, MD 21250 USA, and also with the Department of Computer Science and Information Management, Providence University, Taichung 092912, Taiwan (e-mail: cchang@umbc.edu). Digital Object Identifier 10.1109/TGRS.2022.3186612

PBSF-UBS	Progressive fusion of uniformly selected bands.
R-AD	Correlation matrix-based anomaly detector.
ROC	Receiver operating characteristic.
RT	Real time.
SBF	Sequential band fusion.
SBFS	Sequential backward floating algorithm.
SBSF	Sequential band subset fusion.
SFFS	Sequential forward floating algorithm.
TD	Target detectability.
TDBS	Target detection and BKG suppression.
UBS	Uniform band selection.
VD	Virtual dimensionality.

I. INTRODUCTION

BF has been around for some time but has not received as much attention as BS does. It is quite different from BS in three crucial aspects. One is their functionalities. More specifically, BF intends to integrate spectral information as opposed to BS that tries to remove redundant spectral information. Another is their applications where BF is used for data fusion compared to BS that is spectral dimensionality reduction (DR). A third one is their processed information where BF processes data in RT progressively by fusing bands to integrate spectral information, while BS selects a set of appropriate bands to represent the data, so as to achieve band efficiency after all bands are acquired. A fourth one is their implementation where BF starts with a few initial bands and then fuses more bands until it reaches a satisfactory performance compared to BS that selects a predetermined number of appropriate bands from the entire full bands. Nevertheless, in spite of these differences, both BF and BS share similar design rationales in terms of how bands are fused corresponding to how bands are selected as follows.

In general, there are two ways to design and develop BS algorithms [1], [2]. One is sequential BS (SBS) that implements the SFFS or SBFS developed in [3] to find desired bands one band at a time in a forward or backward manner according to a certain BS criterion. Another is BSS that selects multiple bands simultaneously, such as band clustering/combinations and band subset finding. In BF, a recent work in [4], called SBF, was developed in a similar fashion that a sequential floating forward or backward algorithm can be designed to fuse desired bands one band at a time in a forward and backward manner in parallel to SFFS and SBFS used by SBS.

However, it is interesting to note that there is no counterpart of BSS found for BF reported in the literature. This article fills in this gap by developing PBSF in correspondence to BSS.

In SBS, one general approach is to select bands ranked by a BP criterion sequentially one band at a time based on their calculated priority scores [5]. Such SBS is referred to as BP-SBS where all bands must be prioritized. Another is to implement a BS search strategy, in which case BS can be implemented by either SFFS or SBFS to select a predetermined number of bands [6]–[9]. This type of SBS is referred to as BS-SBS. The difference between these two is that BS-SBS does not necessarily run through all bands, but, instead, it needs to know the number of bands to be selected, n_{BS} beforehand.

Following similar ideas to BP and SFFS/SBFS, Song *et al.* [4] developed four versions of SBF with BP-SBF and BS-SBF as counterparts of BP-SBS and BS-SBS. It particularly took advantage of the BSQ acquisition format by a hyperspectral imaging sensor [10], [11] to perform BF sequentially. As a result of such SBF, it offers sequential changes in spectral profiles across the wavelength range so that the performance of each band can be evaluated band-by-band for data analysis in RT. Then, appropriate bands can be selected and terminated according to their corresponding sequential band profiles, while the bands are acquired at the same time simultaneously.

Unfortunately, SBS suffers from the band correlation issue in the sense that, if a band is selected, then its adjacent bands will be very likely to be selected as well. To resolve this issue, BSS [12]–[15] is developed to consider selected bands as a band subset or band combinations [16]–[18] as a whole band package so that band correlation among selected bands can be taken care of by BSS. Since SBF uses a similar idea to SBS by sequentially selecting one band at a time to be added to the previously selected band set to fuse one band at a time with an already fused band subset, an interesting question arises: “can we also extend SBF in a similar manner that SBS to BSS by fusing band subsets rather than a single band fused with a band subset?” To answer this question, we need to look into how BSS resolves the issue of band correlation. It exhausts all the possible band subsets or combinations for a given n_{BS} , a task that is practically impossible. As a result, all the BSS methods are indeed suboptimal and produce approximate solutions. To translate this issue to BF, we need to deal with band correlation between two-band subsets, particularly the fusion of one band subset with another already fused band subset. Apparently, direct use of the same treatment that extends SBF to SBSF is not applicable to MBS fusion since SBSF requires knowing how many band subsets needed to be fused and also their sequential orders, i.e., the priorities of band subsets to be fused. This issue goes back to exactly the same issue that BSS faces where all possible MBSs to be fused must be exhausted and ranked for their prioritized orders.

This article reinvents the wheel by deviating from the idea of BSS. It introduces a new concept of PBSF that fuses two-band subsets at a time progressively, so as to achieve MBS fusion. In addition, it also takes advantage of UBS to develop PBSF-UBS that can fuse UBS to run through different

bands for its initialization. The central idea of PBSF-MBS is to fuse MBSs. Thus, it does not need to determine the number of bands to be fused as BS does but rather the number of band subsets and their progressive orders to be fused. This is a key difference between PBSF and BS. On the contrary, to implement PBSF-UBS, it does require the number of bands needed to be selected uniformly. Nevertheless, neither BP nor BS is involved in PBSF-MBS or PBSF-UBS. This is a key difference between PBSF and BS. Accordingly, applications in SBF/SBSF are quite different from that in PBSF.

There are three salient differences between SBF/SBSF and PBSF. One is that SBF/SBSF requires BP or BS to select bands to be fused, whereas PBSF does not. A second one is that SBF/SBSF is mainly used in post-band processing as opposed to PBSF, which can be used for hyperspectral data communication and transmission, an area that has yet to be investigated in the future in hyperspectral data exploitation, specifically, hyperspectral satellite communication. For example, transmitting enormous hyperspectral data from a remote site, such as space-borne satellites or airborne aircraft or drones down to receiving stations on the Earth, presents a great challenge due to limited bandwidth. PBSF provides a feasible solution by communicating data in RT progressively instead of transmitting all data simultaneously. In addition, by means of MBS fusion, PBSF allows receiving stations to download data with predetermined specific band subsets and fuse their results with other band subsets currently being acquired. This cannot be done by BS or SBF/SBSF. Finally, the most and significant difference is that SBF/SBSF fuses a single band with a band subset, whereas PBSF fused two different band subsets, which yields results identical to that obtained by directly combining band subsets. This indicates that there is no need of waiting for all bands to be completely acquired.

There is also one key idea of PBSF that cannot be found in BS. That is, its fusion process takes place in its processor's architecture, not data. This is why PBSF can be implemented in RT progressively. It also distinguishes itself from data fusion that fuses data acquired by different sensors at the same time. Therefore, PBSF is heavily determined by a processor used for a particular application. In this article, AD is selected for our application. In this case, PSBF is operated on a selected AD, which is the well-known covariance matrix-based AD developed by Reed and Xiaoli [19], referred to as RX-AD, and also on a correlation matrix-based ADs developed in [20], referred to as R-AD with mathematical derivations and proofs provided in [21] and [22]. Most importantly, by virtue of PBSF, data collection and fusion can be carried out at the same time in a sequential or progressive manner without waiting for completing data acquisition. This cannot be achieved by data fusion and BS.

Several contributions derived from PBSF are summarized as follows.

- 1) In order to ensure that the results of fusing different bands by PBSF are identical to the result using their joint bands, theoretical derivations and mathematical proofs are provided.
- 2) Two versions of PBSF, PBSF-MBS, and PBSF-UBS are developed for PBSF.

- 3) To implement the fusion of two-band subsets, three versions are also derived: BSQ format processed PBSF (PBSF-BSQ), RT-processed PBSF (PBSF-RT), and zigzag-processed PBSF (PBSF-zigzag).
- 4) PBSF offers RT capability that provides progressive spectral profiles of MBSs to be fused. In this case, each band subset can be evaluated and analyzed based on its corresponding spectral performance to determine its significance.
- 5) PBSF enables users to deal with limited bandwidth of data transmission, storage constraints, and data processing effectiveness and efficiency for data communication and transmission with band subsets selected at the disposal of users for fusion.

II. MATHEMATICAL DERIVATIONS OF FUSING TWO-BAND SUBSETS FOR ANOMALY DETECTION

Since PBSF is developed to fuse data of different bands during data acquisition by a sensor, its fusion will take place in the architecture of the processor to be specified by applications. Due to nature of anomalies that generally appear and vanish from time to time, detecting anomalies on a timely basis is critical. This certainly cannot be accomplished by BS. Accordingly, in this section, AD is selected to demonstrate its application due to the fact that AD is one of the fundamental tasks and has shown a great success in hyperspectral data exploitation. AD is quite different from target detection in several aspects. First, according to Chang [10], [21], AD is a passive target detection, which does not need any type of prior target knowledge, while target detection is an active target detection, which requires the knowledge of known targets to be detected. Second, compared to known targets, anomalies are unknown and generally characterized by four unique properties. One is that anomalies cannot be known by prior knowledge or visual inspection. Another is that the presence of anomalies is unexpected and has a low probability. A third one is that anomalies usually occur at the subpixel level with no spatial information. Finally and most importantly, once anomalies are present, their population is relatively small, and thus, anomalies cannot be characterized by Gaussian distributions. Detailed discussions on anomalies can be found in [21] and [22].

Despite that many approaches have been reported in the literature for AD, they are mainly designed and developed based on two classic ADs. One is RX-AD developed in [19] and given by

$$\delta^{\text{RX-AD}}(\mathbf{r}) = (\mathbf{r} - \mu)^T \mathbf{K}_{L \times L}^{-1} (\mathbf{r} - \mu) \quad (1)$$

where $\mathbf{r} \in \mathfrak{R}^{L \times 1}$ is a data sample currently being processed, μ is the sample mean of the image, $\mathbf{K}_{L \times L} \in \mathfrak{R}^{L \times L}$ is the global sample data covariance matrix given by $\mathbf{K}_{L \times L} = (1/N) \sum_{i=1}^N (\mathbf{r}_i - \mu)(\mathbf{r}_i - \mu)^T$, N is the total number of pixels, and L is the total number of bands. Since RX-AD in (1) uses the covariance matrix $\mathbf{K}_{L \times L}$, it is called the covariance $\mathbf{K}_{L \times L}$ -based AD, referred to as K-AD. The RX-AD specified by (1) was derived from the generalized likelihood ratio test based on a binary composite hypothesis problem where the probability distributions of hypotheses were assumed to be

Gaussian. As result, RX-AD turns out to be the Mahalanobis distance. For detailed derivations, we refer to [21] and [22].

The other is correlation sample matrix R-based AD, R-AD, but, recently, it has been shown to be a special case of the constrained energy minimization AD (CEM-AD) in [22] given by

$$\delta^{\text{CEM-AD}}(\mathbf{r}) = \kappa \mathbf{r}^T \mathbf{R}_{L \times L}^{-1} \mathbf{r} \quad (2)$$

where $\mathbf{r} \in \mathfrak{R}^{L \times 1}$ is a data sample currently being processed and $\mathbf{R}_{L \times L} \in \mathfrak{R}^{L \times L}$ is the global sample correlation matrix given by $\mathbf{R}_{L \times L} = (1/N) \sum_{i=1}^N \mathbf{r}_i \mathbf{r}_i^T$. As a result, R-AD can be obtained by (2) with $\kappa = 1$, also called correlation-AD. Of particular interest is R-AD that can be easily implemented as a recursive form to be used for BF [2]. Due to the fact that

$$\mathbf{K}_{L \times L} = \mathbf{R}_{L \times L} - \mu \mu^T. \quad (3)$$

K-AD can be actually realized by R-AD. Because of (3), only R-AD is discussed in this article.

This section presents the BF of any arbitrary pair of two disjoint band subsets, which is the key concept of implementing PBSF. It should be noted that, if two-band subsets have overlapped bands, we can simply remove the overlapped bands from one band subset to make two-band subsets disjoint. Thus, without loss of generality, we assume that two-band subsets to be fused are disjoint thereafter.

Assume that there is another band set, $\mathbf{B}_{t,n} = \{\mathbf{b}_{t_1}, \mathbf{b}_{t_2}, \dots, \mathbf{b}_{t_n}\}$. Then, the data matrix using the two-band sets, $\mathbf{B}_{s,m} = \{\mathbf{b}_{s_1}, \mathbf{b}_{s_2}, \dots, \mathbf{b}_{s_m}\}$ and $\mathbf{B}_{t,n} = \{\mathbf{b}_{t_1}, \mathbf{b}_{t_2}, \dots, \mathbf{b}_{t_n}\}$, can be represented by

$$\mathbf{X}_{\mathbf{B}_{s,m} \mathbf{B}_{t,n}} = \begin{bmatrix} \mathbf{X}_{\mathbf{B}_{s,m}} \\ \mathbf{X}_{\mathbf{B}_{t,n}} \end{bmatrix} = \begin{bmatrix} r_{1s_1} & r_{2s_1} & \cdots & r_{(N-1)s_1} & r_{Ns_1} \\ \vdots & \vdots & \vdots & \vdots & \vdots \\ r_{1s_m} & r_{2s_m} & \cdots & r_{(N-1)s_m} & r_{Ns_m} \\ r_{1t_1} & r_{2t_1} & \cdots & r_{(N-1)t_1} & r_{Nt_1} \\ \vdots & \vdots & \cdots & \vdots & \vdots \\ r_{1t_n} & r_{2t_n} & \cdots & r_{(N-1)t_n} & r_{Nt_n} \end{bmatrix} \quad (4)$$

$$\begin{aligned} \mathbf{R}_{\mathbf{B}_{s,m} \mathbf{B}_{t,n}} &= (m+n)^{-1} \mathbf{X}_{\mathbf{B}_{s,m} \mathbf{B}_{t,n}} \mathbf{X}_{\mathbf{B}_{s,m} \mathbf{B}_{t,n}}^T \\ &= N^{-1} \begin{bmatrix} \mathbf{X}_{\mathbf{B}_{s,n}} \mathbf{X}_{\mathbf{B}_{s,n}}^T & \mathbf{X}_{\mathbf{B}_{s,n}} \mathbf{X}_{\mathbf{B}_{t,n}}^T \\ \mathbf{X}_{\mathbf{B}_{t,n}} \mathbf{X}_{\mathbf{B}_{s,n}}^T & \mathbf{X}_{\mathbf{B}_{t,n}} \mathbf{X}_{\mathbf{B}_{t,n}}^T \end{bmatrix} \end{aligned} \quad (5)$$

$$\mathbf{R}_{\mathbf{B}_{s,m} \mathbf{B}_{t,n}}^{-1} = N \begin{bmatrix} \mathbf{X}_{\mathbf{B}_{s,n}} \mathbf{X}_{\mathbf{B}_{s,n}}^T & \mathbf{X}_{\mathbf{B}_{s,n}} \mathbf{X}_{\mathbf{B}_{t,n}}^T \\ \mathbf{X}_{\mathbf{B}_{t,n}} \mathbf{X}_{\mathbf{B}_{s,n}}^T & \mathbf{X}_{\mathbf{B}_{t,n}} \mathbf{X}_{\mathbf{B}_{t,n}}^T \end{bmatrix}^{-1}. \quad (6)$$

Then, the $(\mathbf{B}_{s,m}, \mathbf{B}_{t,n})$ -fused AD is given by $\mathbf{r}_{\mathbf{B}_{s,m} \mathbf{B}_{t,n}}^T \mathbf{R}_{\mathbf{B}_{s,m} \mathbf{B}_{t,n}}^{-1} \mathbf{r}_{\mathbf{B}_{s,m} \mathbf{B}_{t,n}}$ in terms of $\mathbf{r}_{\mathbf{B}_{s,m}}^T \mathbf{R}_{\mathbf{B}_{s,m}}^{-1} \mathbf{r}_{\mathbf{B}_{s,m}}$ and $\mathbf{r}_{\mathbf{B}_{t,n}}^T \mathbf{R}_{\mathbf{B}_{t,n}}^{-1} \mathbf{r}_{\mathbf{B}_{t,n}}$, where $\mathbf{r}_{\mathbf{B}_{s,m} \mathbf{B}_{t,n}} = (\mathbf{r}_{\mathbf{B}_{s,m}}^T, \mathbf{r}_{\mathbf{B}_{t,n}}^T)^T$. Its recursive equation is given by with detailed derivations provided in the Appendix

$$\begin{aligned} \delta_{\mathbf{B}_{s,m} \mathbf{B}_{t,n}}^{\text{R-AD}} &= \delta_{\mathbf{B}_{s,m}}^{\text{R-AD}} + \frac{1}{N} \left(\mathbf{r}_{\mathbf{B}_{s,m}}^T v_{\mathbf{B}_{s,m} \mathbf{B}_{t,n} | \mathbf{B}_{s,m}} - N \mathbf{r}_{\mathbf{B}_{t,n}}^T \right) \beta_{\mathbf{B}_{s,m} \mathbf{B}_{t,n} | \mathbf{B}_{s,m}} \\ &\quad \times \left(\mathbf{r}_{\mathbf{B}_{s,m} \mathbf{B}_{t,n} | \mathbf{B}_{s,m}}^T \mathbf{r}_{\mathbf{B}_{s,m}} - N \mathbf{r}_{\mathbf{B}_{t,n}}^T \right) \end{aligned} \quad (7)$$

where κ is a constant resulting from the signal-to-noise ratio approach derived in [23], $v_{\mathbf{B}_{s,m} \mathbf{B}_{t,n} | \mathbf{B}_{s,m}} = \mathbf{R}_{\mathbf{B}_{s,m}}^{-1} \mathbf{X}_{\mathbf{B}_{s,m}} \mathbf{X}_{\mathbf{B}_{t,n}}$, and

$\beta_{\mathbf{B}_{s,m}\mathbf{B}_{t,n}|\mathbf{B}_{s,m}} = (\mathbf{x}_{\mathbf{B}_{t,n}}^T [P_{\mathbf{X}_{\mathbf{B}_{s,m}}}^\perp] \mathbf{x}_{\mathbf{B}_{t,n}})^{-1}$ with detailed derivation provided in the Appendix.

The novelties of this section are theoretical derivations, and mathematical proofs of fusing MBSs for AD are completely new and have never been derived.

III. PROGRESSIVE BAND SUBSET FUSION OF UNIFORM BAND SELECTION

PBSF is different from SBF in the sense that it fuses any arbitrary pair of two disjoint band subsets and then can be further extended to fuse multiple disjoint band subsets two at a time progressively. It utilizes the fusion technique developed for two-band subsets in Section II to allow users to fuse band subsets of interest, which are not necessarily selected by BP or BS. In other words, the band subsets to be fused by PBSF can be arbitrary, such as visible bands fused with near-infrared bands, shortwave infrared bands, or bands in specific wavelengths of interest and so on. Such PBSF has great potential in the future hyperspectral data communication and transmission operated from unmanned aerial vehicles (UAVs) or satellite platforms where several receiving stations can simultaneously acquire different disjoint bands, and their, respectively, processed results can be further fused by PBSF at the same time without waiting for all full bands completely acquired. Such capability is particularly suitable for RT monitoring in many applications, such as military combat, environmental pollution, food safety and inspection, and law enforcement.

A. Progressive Fusion of Multiple-Band Subsets

As it is designed by (7), PBSF can be also modified to be applicable to fusing any progressive order of J band subsets, $\{\mathbf{B}_j\}_{j=1}^J$. The most significant advantage resulting from PBSF is that PBSF can produce $J-1$ progressive anomaly maps, $\{\text{PAMap}_j\}_{j=2}^J$ by repeatedly implementing PBSF ($J-1$) times for AD, which can be further analyzed along with the J anomaly maps $\{\text{AMap}_j\}_{j=1}^J$ produced by J individual band subsets, and $\{\mathbf{B}_j\}_{j=1}^J$ for comparative and relative performance analysis.

However, when PBSF is implemented, the progressive order of fusing MBSs must be specified as will be demonstrated by experiments conducted in Sections V and VI.

B. Progressive Band Subset Fusion of Uniformly Selected Bands

Another immediate application of PBSF is to fuse bands produced by UBS. It corresponds to uniform sampling in signal processing. According to compressive sensing theory [24], [25], UBS achieves the maximum possible band incoherence and also achieves the maximum entropy from the information theory perspective. Thus, UBS generally performs reasonably well in BS. In analogy with the Nyquist rate, we can also define a similar concept for UBS; the UBS rate is given as

$$R_{\text{UBS}} = \left[\frac{n_{\text{BS}}}{L} \right] \quad (8)$$

where n_{BS} is the number of bands to be selected. Two options can be used to determine $n_{\text{UBS}}^{\text{initial}}$: floor by $\lfloor(L/n_{\text{BS}})\rfloor$ and ceiling

by $\lceil(L/n_{\text{BS}})\rceil$ with $\lfloor(L/n_{\text{BS}})\rfloor \leq n_{\text{UBS}}^{\text{initial}} < \lceil(L/n_{\text{BS}})\rceil$. For the case of $\lfloor(L/n_{\text{BS}})\rfloor$, the last band subset may contain more than n_{BS} . For the case of $\lceil(L/n_{\text{BS}})\rceil$, the last band subset may contain bands less than n_{BS} . However, to implement UBS, there are $n_{\text{UBS}}^{\text{initial}}$ possible different initial bands, denoted by $\{\mathbf{B}_j^{\text{initial}}\}_{j=1}^{n_{\text{UBS}}^{\text{initial}}}$, each of which can be used to initialize UBS. For the j th initial band, $\mathbf{B}_j^{\text{initial}}$ in $\{\mathbf{B}_j^{\text{initial}}\}_{j=1}^{n_{\text{UBS}}^{\text{initial}}}$ to initialize UBS, a j th band subset, denoted by Bsubset_j can be generated. Accordingly, there are $n_{\text{UBS}}^{\text{initial}}$ different band subsets, $\{\text{Bsubset}_j\}_{j=1}^{n_{\text{UBS}}^{\text{initial}}}$. Since each Bsubset_j yields a different performance, it is highly desirable to take advantage of PBSF to exhaust these $\{\text{Bsubset}_j\}_{j=1}^{n_{\text{UBS}}^{\text{initial}}}$ to run through all possible initial conditions, $\{\mathbf{B}_j^{\text{initial}}\}_{j=1}^{n_{\text{UBS}}^{\text{initial}}}$ by UBS. The resulting PBSF is PBSF of bands uniformly selected by different initial bands and referred to as PBSF-UBS.

For a given progressive order ranked by $\{\mathbf{B}_j^{\text{initial}}\}_{j=1}^{n_{\text{UBS}}^{\text{initial}}}$, there are several ways to fuse $\{\text{Bsubset}_j\}_{j=1}^{n_{\text{UBS}}^{\text{initial}}}$.

- 1) $\{\text{Bsubset}_j\}_{j=1}^{n_{\text{UBS}}^{\text{initial}}}$ is fused by $\{\mathbf{B}_j^{\text{initial}}\}_{j=1}^{n_{\text{UBS}}^{\text{initial}}}$ in a forward manner from $j = 1$ to $n_{\text{UBS}}^{\text{initial}}$. This scenario turns out to be exactly the same as the PBSF-RT to be presented in Section IV-B.
- 2) $\{\text{Bsubset}_j\}_{j=1}^{n_{\text{UBS}}^{\text{initial}}}$ is fused by $\{\mathbf{B}_j^{\text{initial}}\}_{j=1}^{n_{\text{UBS}}^{\text{initial}}}$ in a backward manner from $j = n_{\text{UBS}}^{\text{initial}}$ down to 1.
- 3) $\{\text{Bsubset}_j\}_{j=1}^{n_{\text{UBS}}^{\text{initial}}}$ is fused by $\{\mathbf{B}_j^{\text{initial}}\}_{j=1}^{n_{\text{UBS}}^{\text{initial}}}$ in an alternating forward and backward manner from $j = 1, n_{\text{UBS}}^{\text{initial}}, 2, n_{\text{UBS}}^{\text{initial}} - 1, \dots, \lceil n_{\text{UBS}}^{\text{initial}} / 2 \rceil$.
- 4) $\{\text{Bsubset}_j\}_{j=1}^{n_{\text{UBS}}^{\text{initial}}}$ is fused by $\{\mathbf{B}_j^{\text{initial}}\}_{j=1}^{n_{\text{UBS}}^{\text{initial}}}$ in a midway manner from $j = 1, \lceil n_{\text{UBS}}^{\text{initial}} / 2 \rceil, 2, \lceil n_{\text{UBS}}^{\text{initial}} / 2 \rceil + 1, \dots$ until whichever $\lceil n_{\text{UBS}}^{\text{initial}} / 2 \rceil - 1$ or $n_{\text{UBS}}^{\text{initial}}$ reaches first.
- 5) $\{\text{Bsubset}_j\}_{j=1}^{n_{\text{UBS}}^{\text{initial}}}$ is fused by $\{\mathbf{B}_j^{\text{initial}}\}_{j=1}^{n_{\text{UBS}}^{\text{initial}}}$ in an arbitrary order.

Since UBS does not need any prior knowledge or BS criteria or BS search algorithms, it can be implemented in RT. In addition, different initial bands used to initialize UBS yield different results. This leads to an issue of which initial band should be used by UBS to yield the best performance. PBSF-UBS resolves this dilemma by fusing them all. The other is that PBSF of UBS shares a similar idea to the exhaustive uniform band sampling developed in [26].

The developments of PBSF-MBS and PBSF-UBS in this section are considered as novelties and have never been explored in hyperspectral band processing.

IV. VARIOUS VERSIONS OF FUSING TWO-BAND SUBSETS FOR PBSF

Since a band subset consists of more than one band, when two-band subsets are fused, how to fuse individual bands in both band subsets is an interesting issue arising in PBSF that does not exist in SBF. This is because SBF always fuses one single band with the previously fused band subset. Thus, in what follows, we describe three different ways to perform p band subsets.

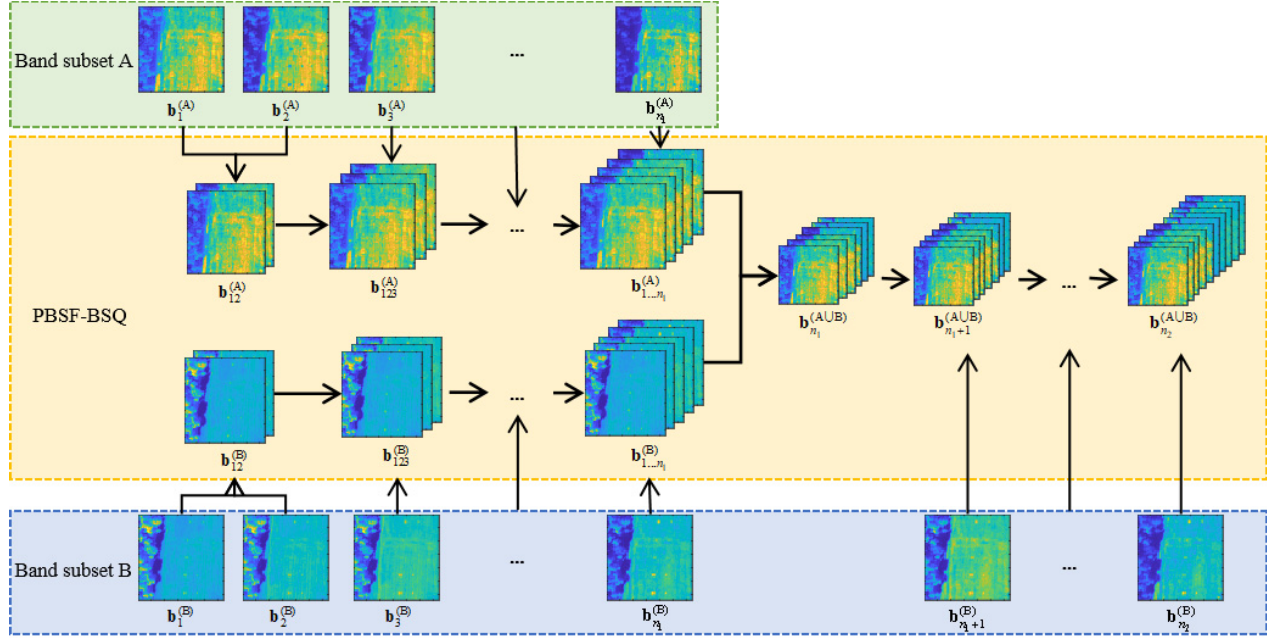


Fig. 1. Schematic of PBSF-BSQ.

A. PBSF-Band Sequential

One immediate approach is to extend SBF-BSQ in [4] to PBSF-BSQ where two BF stage processes are involved. The first BF stage process is carried out by fusing the bands in each of p band subsets in parallel simultaneously by BSQ. It is then followed by the second BF stage process, which fuses p band subsets progressively discussed in Section III.

Using two-band subsets as an illustrative example, let two-band subsets, $\Omega^{(A)} = \{b_l^{(A)}\}_{l=1}^{n_1}$ and $\Omega^{(B)} = \{b_l^{(B)}\}_{l=1}^{n_2}$, with $n_1 \leq n_2$ without loss of generality. The first BF stage process is to apply BSQ directly to each of the two-band subsets simultaneously as follows:

$$\begin{aligned} b_1^{(A)} \rightarrow b_{12}^{(A)} &= \{b_1^{(A)}\} \cup \{b_2^{(A)}\} \rightarrow b_{123}^{(A)} = \{b_{12}^{(A)}\} \cup b_3^{(A)} \\ &\rightarrow \dots \rightarrow b_{1,...,n_1}^{(A)} = \{b_{1,...,(n_1-1)}^{(A)}\} \cup b_{n_1}^{(A)} \end{aligned}$$

and

$$\begin{aligned} b_1^{(B)} \rightarrow b_{12}^{(B)} &= \{b_1^{(B)}\} \cup \{b_2^{(B)}\} \rightarrow b_{123}^{(B)} = \{b_{12}^{(B)}\} \cup b_3^{(B)} \\ &\rightarrow \dots \rightarrow b_{1,...,n_1}^{(B)} = \{b_{1,...,(n_1-1)}^{(B)}\} \cup b_{n_1}^{(B)} \end{aligned}$$

are fused in parallel.

After bands are run out in the band subset A , the fusion will take place, and the remaining bands in the band subset B by SBF

$$\begin{aligned} b_{n_1}^{(A\cup B)} &= \{b_{1,...,n_1}^{(B)}\} \cup b_{n_1}^{(A)} \rightarrow b_{n_1+1}^{(A\cup B)} = b_{n_1}^{(A\cup B)} \cup \{b_{n_1+1}^{(B)}\} \\ &\rightarrow \dots \rightarrow b_{n_2}^{(A\cup B)} = \{b_{n_2-1}^{(B)}\} \cup b_{n_2}^{(B)} \end{aligned}$$

are then fused. Fig. 1 depicts a schematic of fusing two-band subsets, $\Omega^{(A)} = \{b_l^{(A)}\}_{l=1}^{n_1}$ and $\Omega^{(B)} = \{b_l^{(B)}\}_{l=1}^{n_2}$, as described above.

B. PBSF-Real Time

Unlike PBSF-BSQ that fuses p individual band subsets in parallel simultaneously by BSQ, PBSF-RT is carried out by

a single process, which takes place in RT by fusing bands starting from the first bands in each of p band subsets, then the second bands in each of p band subsets, then the second band, and so on. This process can be also illustrated by fusing two-band subsets, $\Omega^{(A)} = \{b_l^{(A)}\}_{l=1}^{n_1}$ and $\Omega^{(B)} = \{b_l^{(B)}\}_{l=1}^{n_2}$, with $n_1 \leq n_2$ as follows:

$$\begin{aligned} b_1^{(A)} \cup b_1^{(B)} &= b_1^{(A\cup B)} \\ b_2^{(A)} \cup b_2^{(B)} &= b_2^{(A\cup B)} \\ \rightarrow b_1^{(A\cup B)} \cup b_2^{(A\cup B)} &= b^{(2)} \rightarrow b_3^{(A)} \cup b_3^{(B)} = b_3^{(A\cup B)} \\ \rightarrow b^{(2)} \cup b_3^{(A\cup B)} &= b^{(3)} \rightarrow b_4^{(A)} \cup b_4^{(B)} = b_4^{(A\cup B)} \\ b^{(3)} \cup b_4^{(A\cup B)} &= b^{(4)} \rightarrow \dots \rightarrow b^{(n_1)} \\ \rightarrow b_{1,...,n_1}^{(B)} &= \{b_{n_1+1}^{(B)}\} \cup b_{n_1}^{(B)}. \end{aligned}$$

After $b_{1,...,n_1}^{(B)}$ is obtained, the fusion will then take place by SBF and the remaining bands in the band subset B

$$b_{n_1+1}^{(B)} \rightarrow \dots \rightarrow b_{n_2}^{(B)} = \{b_{n_2-1}^{(B)}\} \cup b_{n_2}^{(B)}.$$

Fig. 2 shows a schematic of the above process fusing two-band subsets: $\Omega^{(A)} = \{b_l^{(A)}\}_{l=1}^{n_1}$ and $\Omega^{(B)} = \{b_l^{(B)}\}_{l=1}^{n_2}$. Interestingly, PBSF of UBS presented in Section III-B can be also implemented in PBSF-RT if we fuse $\{\text{Bsubset}_j\}_{j=1}^{\text{n}_{\text{UBS}}^{\text{initial}}}$ according to the progressive order ranked by $\{\mathbf{B}_j^{\text{initial}}\}_{j=1}^{\text{n}_{\text{UBS}}^{\text{initial}}}$.

C. PBSF-Zigzag

Since PBSF-RT fuses band subsets as bands are being transmitted and received band-by-band in RT at the p receiving stations simultaneously according to the BSQ format, it does not take care of interband correlation in each band subset. To address this issue, a third approach is derived from an idea similar to JPEG, which decomposes each image into 64×64 blocks with each block compressed by discrete cosine transform (DCT) in a zigzag manner [27], [28]. It is

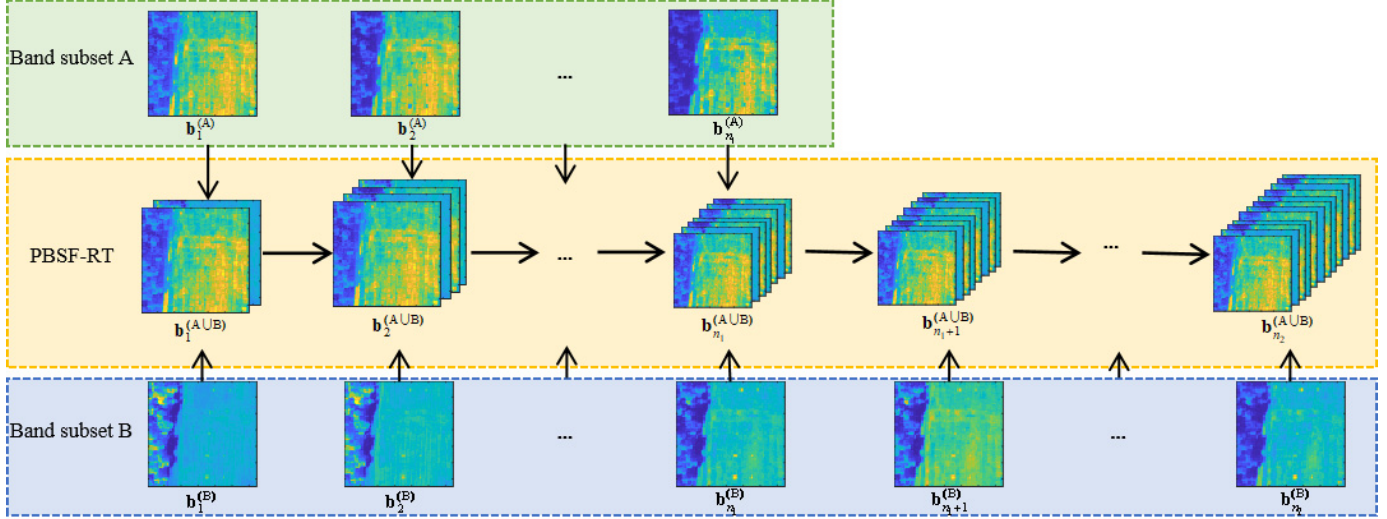


Fig. 2. Schematic of PBSF-RT.

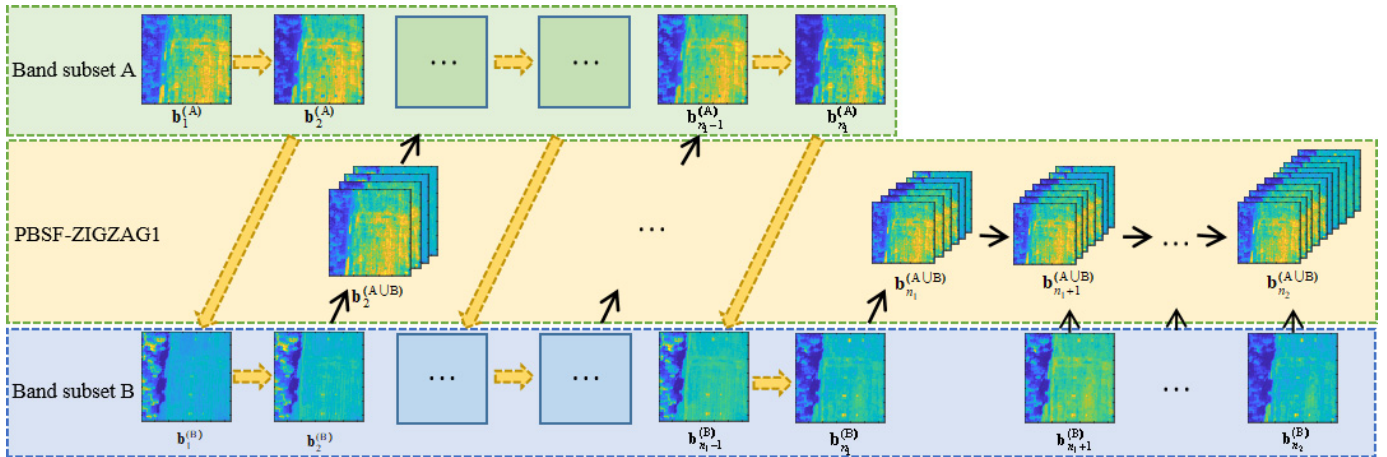


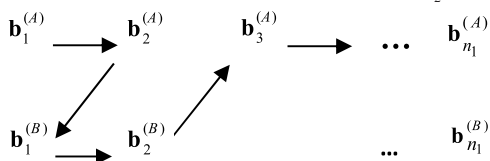
Fig. 3. Schematic of PBSF-zigzag1.

TABLE I
BAND SUBSETS SELECTED FOR VIS, NIR, AND SWIR SPECTRAL RANGES FOR HYDICE DATA IN FIG. 4

Receiving station	Bsubset	Spectral wavelength (nm)	Spectral bands
1	\mathbf{B}_{VIS}	400-750	1-56
2	\mathbf{B}_{NIR}	750-1400	57-97
3	\mathbf{B}_{SWIR}	140-25000	98-169

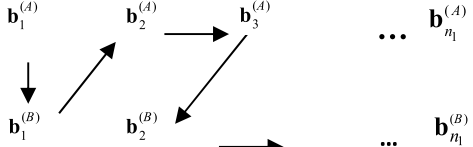
called PBSF-zigzag, which can be considered as a hybrid of PBSF-BSQ and PBSF-RT and can be described in two versions, PBSF-zigzag1 and PBSF-zigzag2, as follows with the schematic of PBSF-zigzag1 fusing two-band subsets: $\Omega^{(A)} = \{\mathbf{b}_l^{(A)}\}_{l=1}^{n_1}$ and $\Omega^{(B)} = \{\mathbf{b}_l^{(B)}\}_{l=1}^{n_2}$.

1) PBSF-zigzag1 processes $\mathbf{b}_1^{(A)}$ \rightarrow $\mathbf{b}_2^{(A)}$ \rightarrow ... \rightarrow $\mathbf{b}_{n_2}^{(A)}$ as follows:



After $\mathbf{b}_{n_1}^{(B)}$, the fusion will then take place by SBF in the band subset B , as shown in Fig. 3 for illustration.

2) PBSF-zigzag2 processes $\mathbf{b}_1^{(A)}$ \rightarrow $\mathbf{b}_2^{(A)}$ \rightarrow ... \rightarrow $\mathbf{b}_{n_2}^{(A)}$ as follows:



After $\mathbf{b}_{n_1}^{(B)}$, the fusion will then take place by SBF in the band subset B .

It should be pointed out that all the results presented in this section are new and have never been reported in the past.

V. 3-D ROC CURVE-DERIVED DETECTION MEASURES

To measure detection performance, the 2-D ROC curve has been commonly used as an evaluation tool. It is a plot

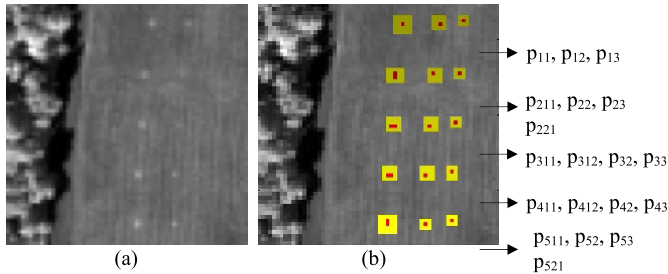


Fig. 4. (a) HYDICE panel scene which contains 15 panels. (b) Ground-truth map of spatial locations of 19 R panel pixels.

of detection probability P_D versus false alarm probability P_F , and then, the area under this curve (AUC), denoted by $AUC_{(D,F)}$, is calculated to assess the effectiveness of a detector. Unfortunately, it has been shown in [29] and also in [21]–[23] that using $AUC_{(D,F)}$ alone often resulted in incorrect final conclusions. The major reason caused by such misleading is simply because both P_D and P_F are calculated by the same threshold τ used by a detector. Consequently, when both P_D and P_F are very high, its calculated $AUC_{(D,F)}$ is also very high. Conversely, when both P_D and P_F are very low, its calculated $AUC_{(D,F)}$ is also very low. More specifically, P_D and P_F are not independent parameters. Accordingly, P_D and P_F cannot individually measure TD and BKG suppressibility (BS), respectively. To resolve this dilemma, Chang [29] developed an effective 3-D ROC analysis-based evaluation tool to extend the traditional 2-D ROC analysis by including the threshold τ as an additional parameter to represent a 3-D ROC curve as a function of three parameters, P_D , P_F , and τ , as a triplet parameter vector specified by (P_D, P_F, τ) . Using this 3-D ROC curve, three 2-D ROC curves of (P_D, P_F) , (P_D, τ) , and (P_F, τ) can be, therefore, generated with their respective AUC values, denoted by $AUC_{(D,F)}$, $AUC_{(D,\tau)}$, and $AUC_{(F,\tau)}$. In this case, $AUC_{(D,\tau)}$ and $AUC_{(F,\tau)}$ can be used to evaluate TD and BS, respectively. In addition to these three AUC values, five new AUC measures developed in [29] to measure joint TD, joint BS, TDBS, the signal-to-noise probability ratio (SNPR), and overall detection probability (ODP) can be also defined in the following.

- 1) $AUC_{(D,F)}$: Effectiveness of a detector.
- 2) $AUC_{(D,\tau)}$: TD of a detector.
- 3) $AUC_{(F,\tau)}$: BS of a detector.
- 4) AUC_{TD} : Joint TD of a detector is defined by

$$0 \leq AUC_{TD} = AUC_{(D,F)} + AUC_{(D,\tau)} \leq 2. \quad (9)$$

- 5) AUC_{BS} : Joint BS of the detector is defined by

$$-1 \leq AUC_{BS} = AUC_{(D,F)} - AUC_{(F,\tau)} \leq 1. \quad (10)$$

- 6) AUC_{TDBS} : TDBS of a detector is defined by

$$-1 \leq AUC_{TDBS} = AUC_{(D,\tau)} - AUC_{(F,\tau)} \leq 1. \quad (11)$$

- 7) AUC_{SNPR} : SNPR of a detector is defined by

$$0 \leq AUC_{SNPR} = \frac{AUC_{(D,\tau)}}{AUC_{(F,\tau)}}. \quad (12)$$

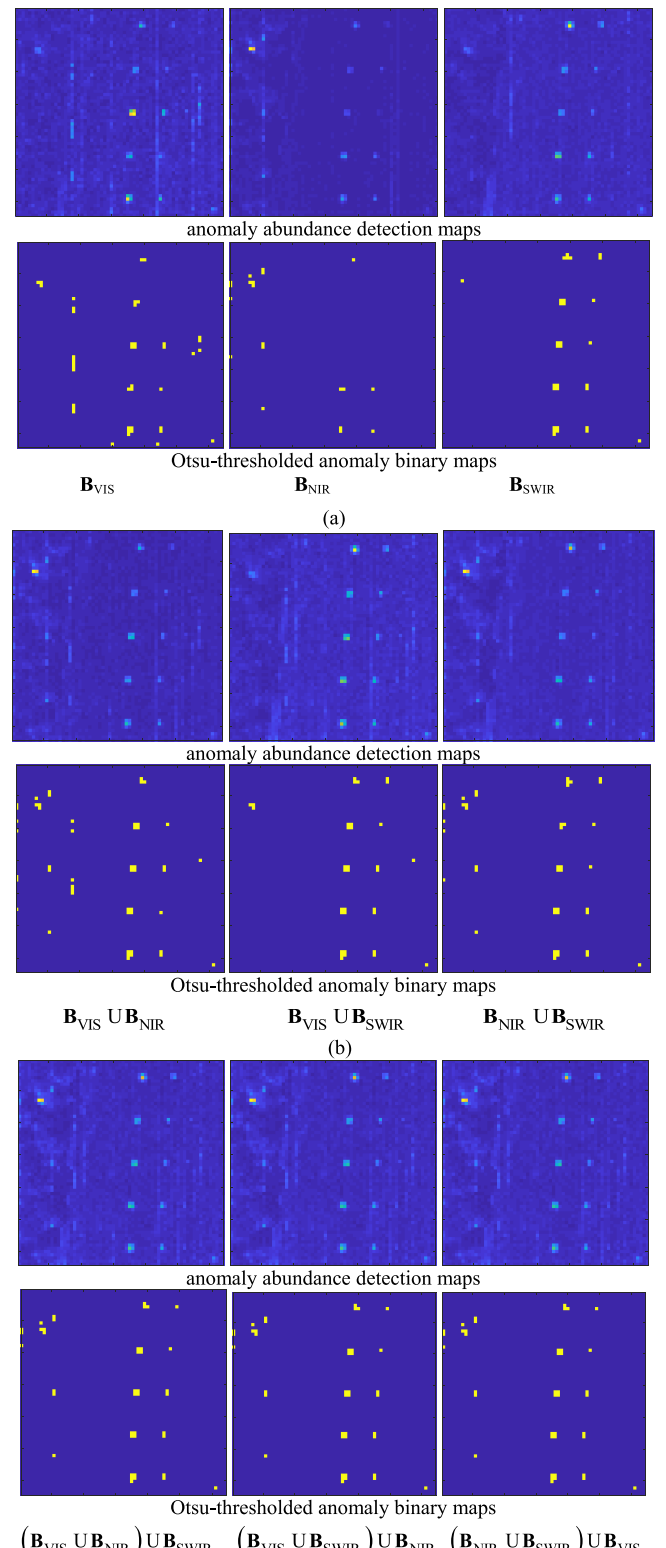


Fig. 5. R-AD detected anomaly abundance maps of different BF sets. (a) R-AD detection results of using single-band subsets. (b) R-AD detection results of fusing two-band subsets. (c) R-AD detection results of fusing three-band subsets.

- 8) AUC_{ODP} : ODP of a detector is defined by

$$\begin{aligned} -1 \leq AUC_{ODP} = & AUC_{(D,F)} \\ & + AUC_{(D,\tau)} - AUC_{(F,\tau)} \leq 2. \end{aligned} \quad (13)$$

TABLE II

VARIOUS AUC VALUES CALCULATED FROM THE THREE 2-D ROC CURVES OF DETECTION RESULTS IN FIG. 7 USING DIFFERENT BAND SUBSETS

Band subsets	AUC _(D,F)	AUC _(D,r)	AUC _(F,r)	AUC _{TD}	AUC _{BS}	AUC _{TDBS}	AUC _{ODP}	AUC _{SNPR}
B_{VIS}	0.9445	0.3661	0.0388	1.3105	0.9056	0.3272	1.2717	9.4288
B_{NIR}	0.9727	0.1424	0.0160	1.1151	0.9567	0.1264	1.0990	8.8886
B_{SWIR}	0.9931	0.3297	0.0355	1.3229	0.9577	0.2943	1.2874	9.2957
B_{VIS} UB_{NIR}	0.9767	0.2392	0.0290	1.2159	0.9477	0.2102	1.1869	8.2552
B_{VIS} UB_{SWIR}	0.9926	0.4192	0.0451	1.4118	0.9474	0.3741	1.3666	9.2877
B_{NIR} UB_{SWIR}	0.9881	0.2797	0.0384	1.2679	0.9498	0.2414	1.2295	7.2875
B_{VIS} UB_{NIR} UB_{SWIR}	0.9894	0.3450	0.0434	1.3344	0.9460	0.3016	1.2910	7.9489

VI. REAL IMAGE EXPERIMENTS OF MULTIPLE BANDS FUSED BY PBSF

An airborne hyperspectral digital imagery collection experiment (HYDICE) scene shown in Fig. 4 was used to demonstrate the full utility of PBSF. The data were collected in August 1995 from a flight altitude of 10 000 ft. There are 15 square panels in Fig. 4(a) with three different sizes, 3 m × 3 m, 2 m × 2 m, and 1 m × 1 m, respectively. Due to the ground sampling distance of approximately 1.56 m, the each of panels in the first column except the first row contains two panel pixels highlighted by red, p_{211} and p_{221} in row 2, p_{311} and p_{321} in row 3, p_{411} and p_{421} in row 4, and p_{511} and p_{521} in row 5, as shown in Fig. 4. All the remaining 11 panels in Fig. 1 contain one single panel pixel for each panel also highlighted by red, p_{11} , p_{12} , and p_{13} in row 1, p_{22} and p_{23} in row 2, p_{32} and p_{33} in row 3, p_{42} and p_{43} in row 4, and p_{52} and p_{53} in row 5. Therefore, there are a total of 19 red panel pixels. Fig. 4(b) shows their precise spatial locations with the pixels in yellow (Y pixels) indicating panel pixels mixed with the BKG. This particular scene was used for subpixel target detection of panel pixels in the third column and mixed target detection of panel pixels highlighted by yellow in the first and second columns. Detailed descriptions of this data scene and discussions on experiments can be found [31, Secs. 9.3 and 9.4], [35], [36].

A. Multiple-Band Fusion by PBSF

The following experiments were particularly designed to show how PBSF fuses MBSs subset-by-subset. It is particularly useful in satellite data transmission due to its limited bandwidth. Assume that there are a number of satellite data receiving stations, each of which can be designated to receive a certain range of spectral wavelengths at the same time. PBSF-MBS allows these stations to receive, process, and fuse all their datasets simultaneously. In this case, there is no need of determining how many bands to be fused but rather determined by spectral ranges of interest.

Generally speaking, a common spectral range used by a hyperspectral imaging spectrometer covers from 400 to 2500 nm. In this case, we can divide this range into three regions of interest: the visible range from 400 to 750 nm, the NIR range from 750 to 1400 nm, and the short-wave infrared (SWIR) range from 1400 to 2500 nm. Let these three-band

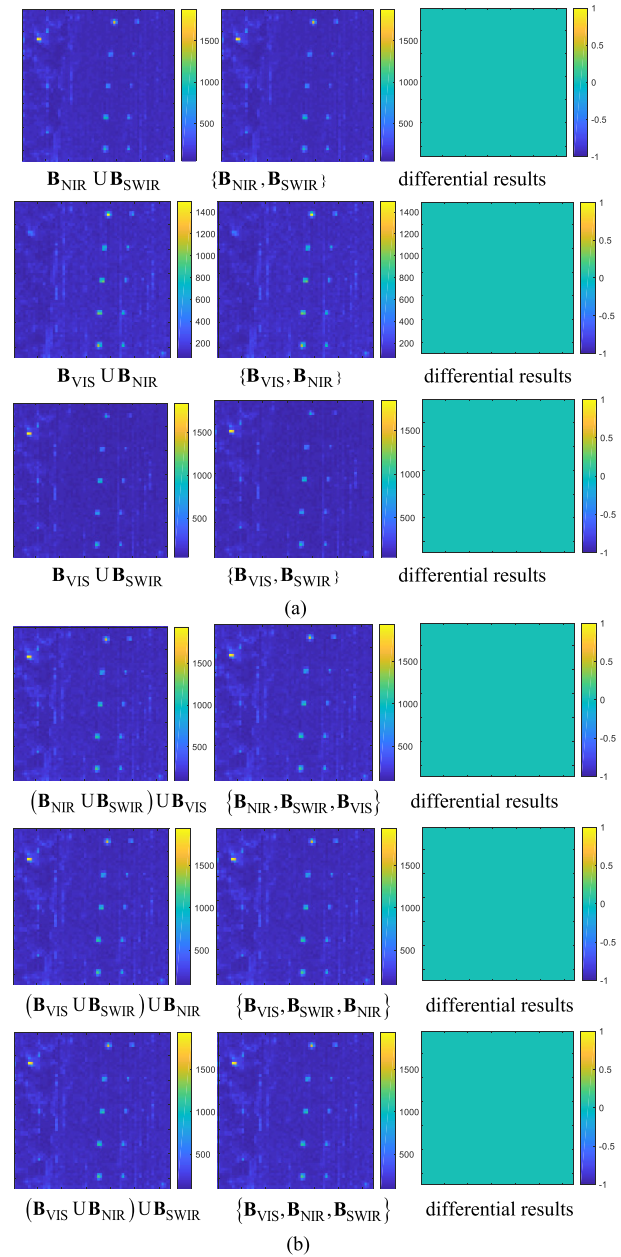


Fig. 6. Validation of fusion equation (7). (a) Fusion of two-band subsets. (b) Fusion of three-band subsets.

subsets be denoted by \mathbf{B}_{VIS} , \mathbf{B}_{NIR} , and \mathbf{B}_{SWIR} with their bands tabulated in Table I, which are assumed to be transmitted to three different receiving stations.

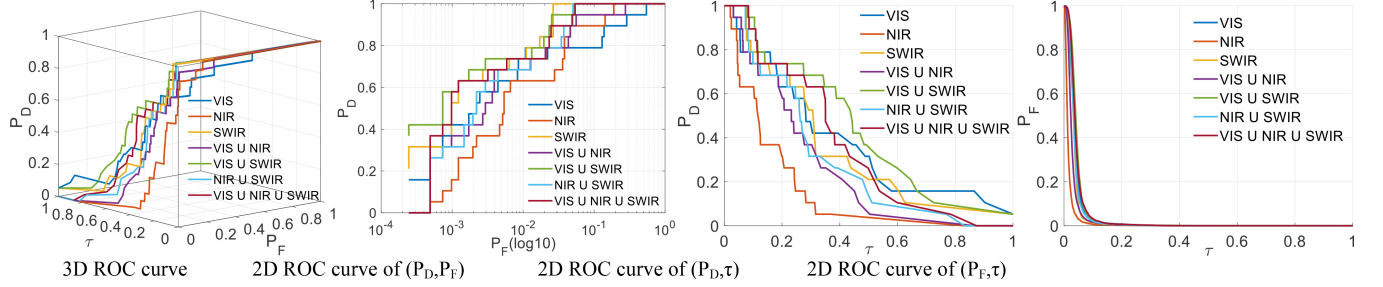


Fig. 7. 3-D ROC curves along with their generated three 2-D ROC curves of R-AD detected anomaly maps of \mathbf{B}_{VIS} , \mathbf{B}_{NIR} , \mathbf{B}_{SWIR} , $\mathbf{B}_{\text{VIS}} \cup \mathbf{B}_{\text{NIR}}$, $\mathbf{B}_{\text{VIS}} \cup \mathbf{B}_{\text{SWIR}}$, and $\mathbf{B}_{\text{NIR}} \cup \mathbf{B}_{\text{SWIR}}$.

TABLE III
BAND SUBSETS SELECTED FOR PBSF-UBS FOR HYDICE DATA IN FIG. 4

Receiving stations	Bsubsets									
1	1	19	38	57	76	94	113	132	151	
2	2	20	39	58	77	95	114	133	152	
3	3	21	40	59	78	96	115	134	153	
4	4	22	41	60	79	97	116	135	154	
5	5	23	42	61	80	98	117	136	155	
6	6	24	43	62	81	99	118	137	156	
7	7	25	44	63	82	100	119	138	157	
8	8	26	45	64	83	101	120	139	158	
9	9	27	46	65	84	102	121	140	159	
10	10	28	47	66	85	103	122	141	160	
11	11	29	48	67	86	104	123	142	161	
12	12	30	49	68	87	105	124	143	162	
13	13	31	50	69	88	106	125	144	163	
14	14	32	51	70	89	107	126	145	164	
15	15	33	52	71	90	108	127	146	165	
16	16	34	53	72	91	109	128	147	166	
17	17	35	54	73	92	110	129	148	167	
18	18	36	55	74	93	111	130	149	168	
19		37	56	75		112	131	150	169	

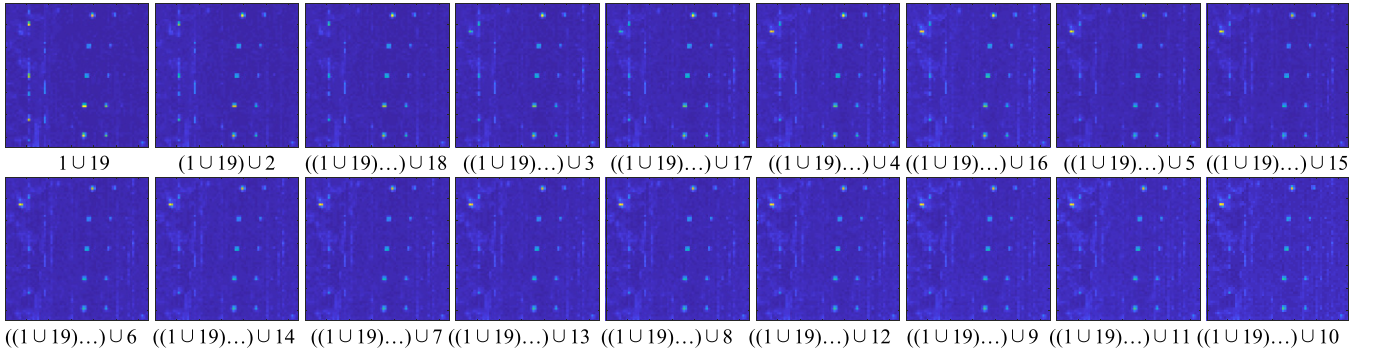


Fig. 8. R-AD detected anomaly maps of different BF subsets.

Three scenarios were performed by PBSF in terms of different progressive orders of fusing these three-band subsets. One is to first fuse \mathbf{B}_{VIS} with \mathbf{B}_{NIR} and then followed by fusing the third band subset, \mathbf{B}_{SWIR} , denoted by $(\mathbf{B}_{\text{VIS}} \cup \mathbf{B}_{\text{NIR}}) \cup \mathbf{B}_{\text{SWIR}}$. A second scenario is to fuse \mathbf{B}_{VIS} with \mathbf{B}_{SWIR} and then followed by fusing with \mathbf{B}_{NIR} , denoted by $(\mathbf{B}_{\text{VIS}} \cup \mathbf{B}_{\text{SWIR}}) \cup \mathbf{B}_{\text{NIR}}$. A third scenario is to first fuse \mathbf{B}_{NIR} with \mathbf{B}_{SWIR} and then followed by fusing with \mathbf{B}_{VIS} , denoted by $(\mathbf{B}_{\text{NIR}} \cup \mathbf{B}_{\text{SWIR}}) \cup \mathbf{B}_{\text{VIS}}$. Fig. 5(a)–(c) shows the anomaly abundance detection maps of R-AD using these three scenarios

along with their anomaly binary maps that were obtained by Otsu's thresholding method [30].

By visual inspection of Fig. 5, using \mathbf{B}_{SWIR} performed better than the other two single-band subsets and nearly the same as PBSF of fusing two or three-band subsets with no visible differences. Interestingly, PBSF fusing three-band subsets did not provide advantages compared to PBSF fusing two-band subsets. The results in Fig. 5 demonstrated that panel signatures could be detected using only SWIR bands. It also showed that, if SWIR bands were not used,

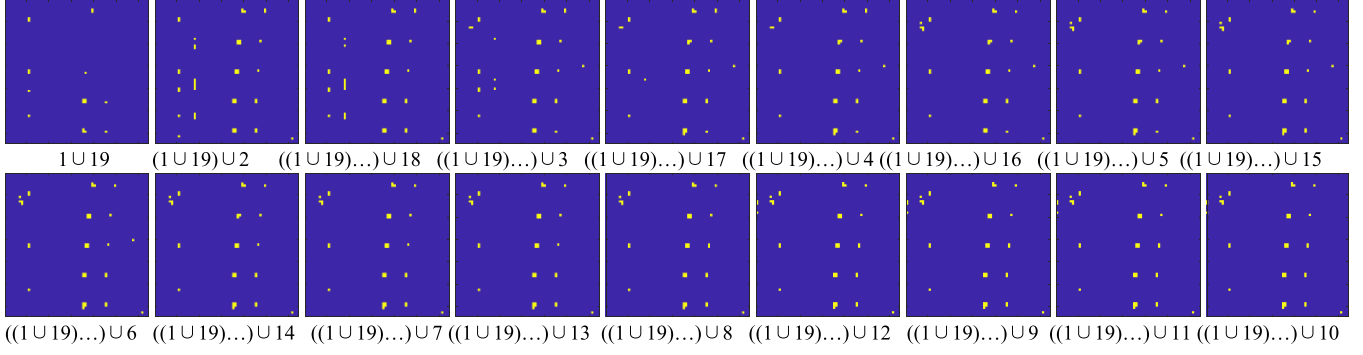


Fig. 9. Binary maps of different BF subsets by Otsu's method.

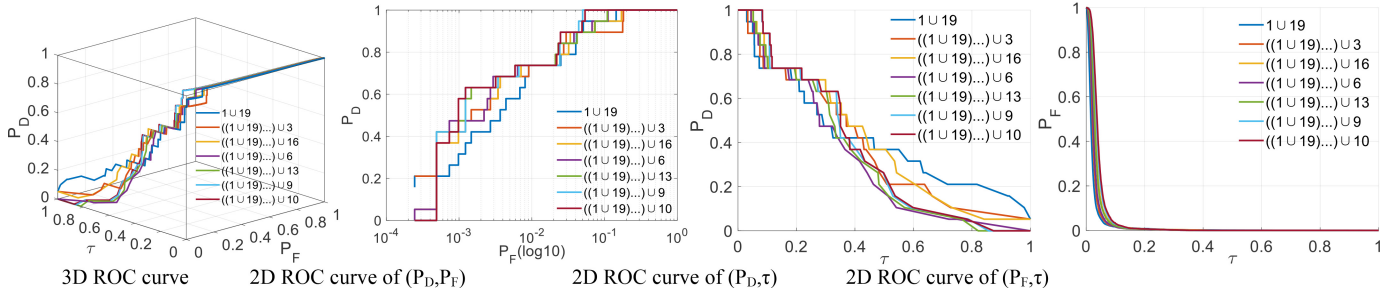


Fig. 10. 3-D ROC curves along with their generated three 2-D ROC curves of R-AD detected anomaly maps by fusing different subsets.

TABLE IV

VARIOUS AUC VALUES CALCULATED FROM THE THREE 2-D ROC CURVES OF DETECTION RESULTS IN FIG. 10 USING DIFFERENT BAND SUBSETS

Band subsets	$AUC_{(D,F)}$	$AUC_{(D,\tau)}$	$AUC_{(F,\tau)}$	AUC_{TD}	AUC_{BS}	AUC_{TDBS}	AUC_{ODP}	AUC_{SNPR}
1 ∪ 19	0.9837	0.4071	0.0225	1.3908	0.9612	0.3846	1.3683	18.1193
(1 ∪ 19) ∪ 2	0.9702	0.3771	0.0242	1.3473	0.9460	0.3529	1.3231	15.5867
((1 ∪ 19) ∪ 2) ∪ 18	0.9812	0.3687	0.0242	1.3499	0.9570	0.3445	1.3257	15.2569
((1 ∪ 19) ∪ ... ∪ 18) ∪ 3	0.9755	0.3661	0.0273	1.3416	0.9482	0.3387	1.3142	13.3958
((1 ∪ 19) ∪ ... ∪ 3) ∪ 17	0.9806	0.3682	0.0289	1.3487	0.9517	0.3393	1.3198	12.7408
((1 ∪ 19) ∪ ... ∪ 17) ∪ 4	0.9757	0.3692	0.0324	1.3449	0.9433	0.3368	1.3125	11.4000
((1 ∪ 19) ∪ ... ∪ 4) ∪ 16	0.9799	0.3882	0.0369	1.3681	0.9430	0.3513	1.3312	10.5186
((1 ∪ 19) ∪ ... ∪ 16) ∪ 5	0.9817	0.2818	0.0265	1.2636	0.9552	0.2553	1.2371	10.6384
((1 ∪ 19) ∪ ... ∪ 5) ∪ 15	0.9846	0.2929	0.0279	1.2774	0.9567	0.2650	1.2495	10.4969
((1 ∪ 19) ∪ ... ∪ 15) ∪ 6	0.9841	0.3018	0.0293	1.2860	0.9548	0.2725	1.2566	10.2962
((1 ∪ 19) ∪ ... ∪ 6) ∪ 14	0.9833	0.3092	0.0316	1.2925	0.9517	0.2776	1.2609	9.7845
((1 ∪ 19) ∪ ... ∪ 14) ∪ 7	0.9849	0.3145	0.0316	1.2994	0.9532	0.2828	1.2677	9.9366
((1 ∪ 19) ∪ ... ∪ 7) ∪ 13	0.9856	0.3197	0.0343	1.3053	0.9512	0.2854	1.2710	9.3153
((1 ∪ 19) ∪ ... ∪ 13) ∪ 8	0.9889	0.3271	0.0352	1.3160	0.9538	0.2919	1.2809	9.2994
((1 ∪ 19) ∪ ... ∪ 8) ∪ 12	0.9883	0.3339	0.0379	1.3222	0.9504	0.2961	1.2843	8.8157
((1 ∪ 19) ∪ ... ∪ 12) ∪ 9	0.9899	0.3403	0.0414	1.3301	0.9485	0.2989	1.2888	8.2277
((1 ∪ 19) ∪ ... ∪ 9) ∪ 11	0.9892	0.3429	0.0440	1.3321	0.9453	0.2989	1.2882	7.8012
((1 ∪ 19) ∪ ... ∪ 11) ∪ 10	0.9894	0.3450	0.0434	1.3344	0.9460	0.3016	1.2910	7.9489

fusing VIS and NIR bands could also do as well as SWIR bands.

In order to validate the fusion equation (7) used for fusing two-band subsets and three-band subsets, Fig. 6(a) and (b) shows their respective fused anomaly abundance maps in the first column, anomaly abundance detection maps of joint band subsets without fusion in the second column, and their differential anomaly maps for the second and third scenarios in the third column where the values of differential results were nearly zeros, which were not zeros because of numerical errors.

In order to further conduct detailed quantitative analysis, the 3-D ROC curve-derived detection measures presented in Section V were used to evaluate the detection performance in Fig. 5. Fig. 7 plots the 3-D ROC curves in \log_{10} of the anomaly abundance detection maps in Fig. 5 along with their corresponding three 2-D ROC curves where R-AD using single-band subset specified by SWIR produced the best AUC value of (P_D, P_F) , denoted by $AUC_{(D,F)}$, while R-AD using fused two-band subsets, $\mathbf{B}_{VIS} \cup \mathbf{B}_{SWIR}$, produced the best AUC value of (P_D, τ) , denoted by $AUC_{(D,\tau)}$. Interestingly, R-AD using single-band subset specified by NIR produced the least

TABLE V
BAND SUBSETS FOR PBSF-BSQ FOR HYDICE DATA IN FIG. 4

Station 1 (Bsubset 1)	Station 2 (Bsubset 2)	Station 3 (Bsubset 3)	Station 4 (Bsubset 4)	Station 5 (Bsubset 5)	Station 6 (Bsubset 6)	Station 7 (Bsubset 7)	Station 8 (Bsubset 8)	Station 9 (Bsubset 9)
1	19	38	57	76	94	113	132	151
2	20	39	58	77	95	114	133	152
3	21	40	59	78	96	115	134	153
4	22	41	60	79	97	116	135	154
5	23	42	61	80	98	117	136	155
6	24	43	62	81	99	118	137	156
7	25	44	63	82	100	119	138	157
8	26	45	64	83	101	120	139	158
9	27	46	65	84	102	121	140	159
10	28	47	66	85	103	122	141	160
11	29	48	67	86	104	123	142	161
12	30	49	68	87	105	124	143	162
13	31	50	69	88	106	125	144	163
14	32	51	70	89	107	126	145	164
15	33	52	71	90	108	127	146	165
16	34	53	72	91	109	128	147	166
17	35	54	73	92	110	129	148	167
18	36	55	74	93	111	130	149	168
	37	56	75		112	131	150	169

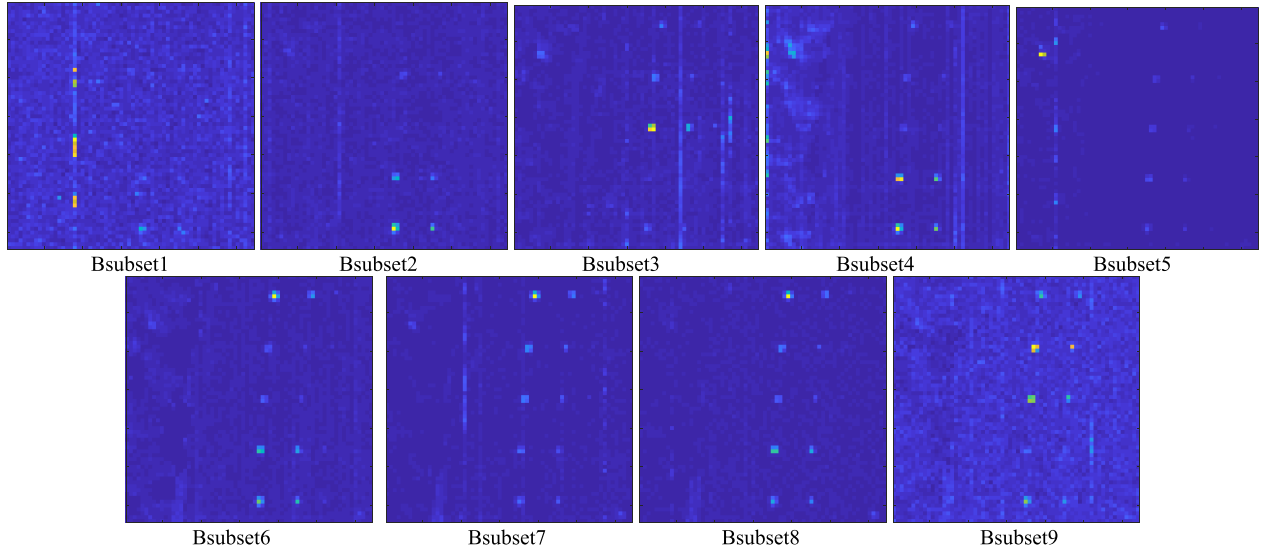


Fig. 11. R-AD detection maps of each receiving station.

AUC value of (P_F, τ) , denoted by $\text{AUC}_{(F, \tau)}$ which indicated the best BS. These results showed that different band subsets offered different advantages of evaluating detection performance. In addition to $\text{AUC}_{(D, F)}$, $\text{AUC}_{(D, \tau)}$, and $\text{AUC}_{(F, \tau)}$, Table II also tabulates the results of five detection measures specified by (9)–(13) for detailed quantitative studies and comparison where the best results were boldfaced and were produced by $\mathbf{B}_{\text{VIS}} \cup \mathbf{B}_{\text{SWIR}}$, which fused the two-band subsets, \mathbf{B}_{VIS} and \mathbf{B}_{SWIR} . This table further demonstrated an important fact that relying only on $\text{AUC}_{(D, F)}$, $\text{AUC}_{(D, \tau)}$, and $\text{AUC}_{(F, \tau)}$ to evaluate AD performance was not sufficient. This is because \mathbf{B}_{SWIR} performed nearly the same as $\mathbf{B}_{\text{VIS}} \cup \mathbf{B}_{\text{SWIR}}$ by visual inspection of Figs. 4 and 5.

B. PBSF of UBS

The next experiments are designed to validate PBSF-UBS. In this case, we need to know the number of bands to be

selected. According to Chang [31], [33] and Chang and Du [32], VD can be used to estimate the number of spectrally distinct signatures. Assume that n_{VD} is the value estimated by VD. Thus, if each signature can be accommodated by one particular spectral band, we only need only n_{VD} bands to differentiate n_{VD} signatures. This also suggests that the entire full band set can be decomposed into n_{VD} band subsets so that one band subset can be distinguished from another and represents particular spectral information, which cannot be offered by other band subsets. For the HYDICE scene in Fig. 4, n_{VD} was estimated to 9 by HFC [34]. Accordingly, $n_{\text{VD}} = 9$ was used to select nine-band subsets to be fused by PBSF for experiments where each band subset is assumed to be able to represent the dataset for AD. To maximize its representation in the sense of maximum band incoherence according to compressive sensing, UBS was used, and each band subset was initialized by a different initial band,

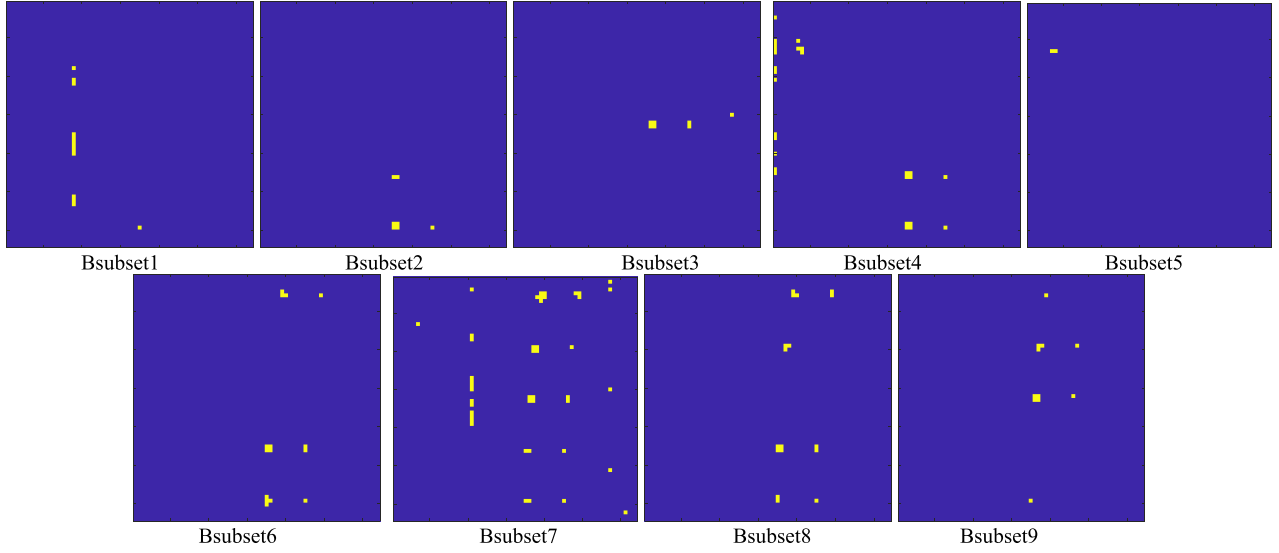


Fig. 12. Binary maps of Fig. 11 thresholded by Otsu's method.

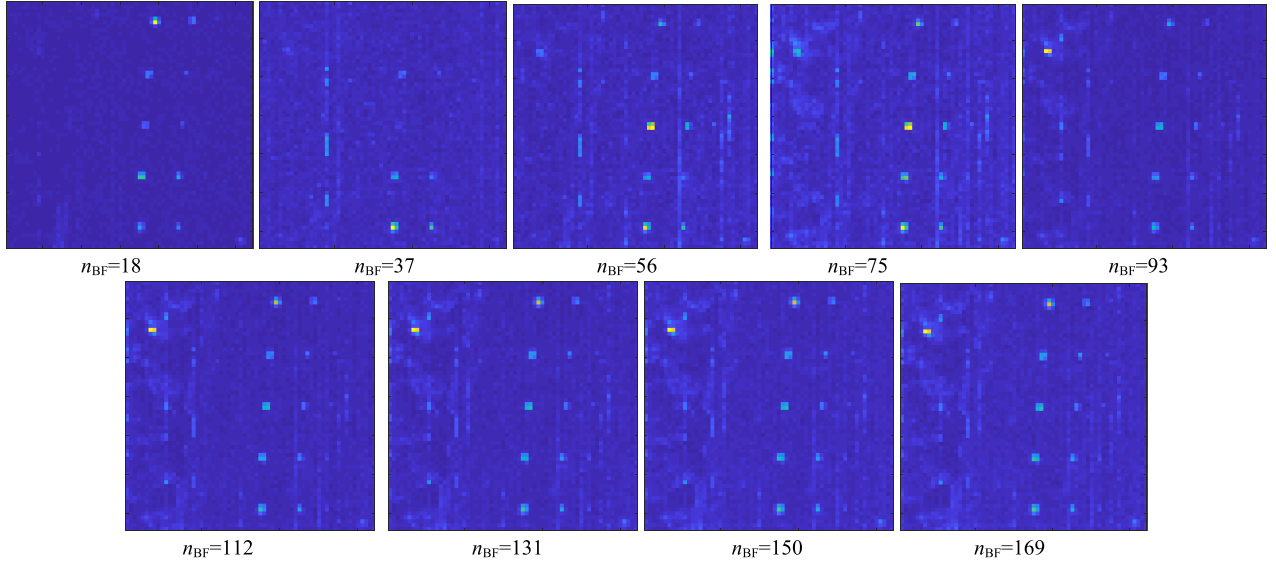


Fig. 13. R-AD detection maps of using PBSF-MBS.

as described in Section III-B. In this case, we can assume that the 169 bands of HYDICE are divided into nine-band subsets and transmitted to the corresponding nine receiving stations, each of which will receive 18 or 19 bands simultaneously. By virtue of PBSF-UBS, we can immediately see the detection results produced by each band subset at the same time and then observe their progressive profiles as more bands in the same band subsets are fused. This unique advantage can be only gained by PBSF but not SBF.

As noted in Section III-B, there are five different scenarios that can be implemented by PBSF of UBS. For an illustrative purpose, we only select scenario 3 for experiments, which fuses the $n_{\text{UBS}}^{\text{initial}}$ MBSs, $\{\text{Bsubset}_j\}_{j=1}^{n_{\text{UBS}}^{\text{initial}}}$ in an alternating forward and backward manner. That is, it first fuses the first UBS band subset (Bsubset1) with the last UBS band subset (Bsubset($n_{\text{UBS}}^{\text{initial}}$))), then second UBS band subset (Bsubset2)

with the second last band subset (Bsubset($n_{\text{UBS}}^{\text{initial}} - 1$)), and so on, until it reached its halfway, $\lceil n_{\text{UBS}}^{\text{initial}}/2 \rceil$, and then, the fusion is completed.

When $n_{\text{BS}} = 9$, $\lceil 169/9 \rceil = 19$, and the last one band subset has only seven bands. In this case, there are 19 receiving stations that are collected synchronously beginning with different initial bands. Except for the last 19th station receiving seven bands, all other 18 receiving stations will receive nine bands. Since $\lceil 19/2 \rceil = 10$, the fusion will be terminated at the tenth band subset, Bsubset10. Table III tabulates 19 receiving stations, each of which receives nine bands according to UBS except the last receiving station, which receives only seven bands. Fig. 8 shows the anomaly abundance detection maps of PBSF implemented by R-AD along with their binary maps thresholded by Otsu's method shown in Fig. 9.

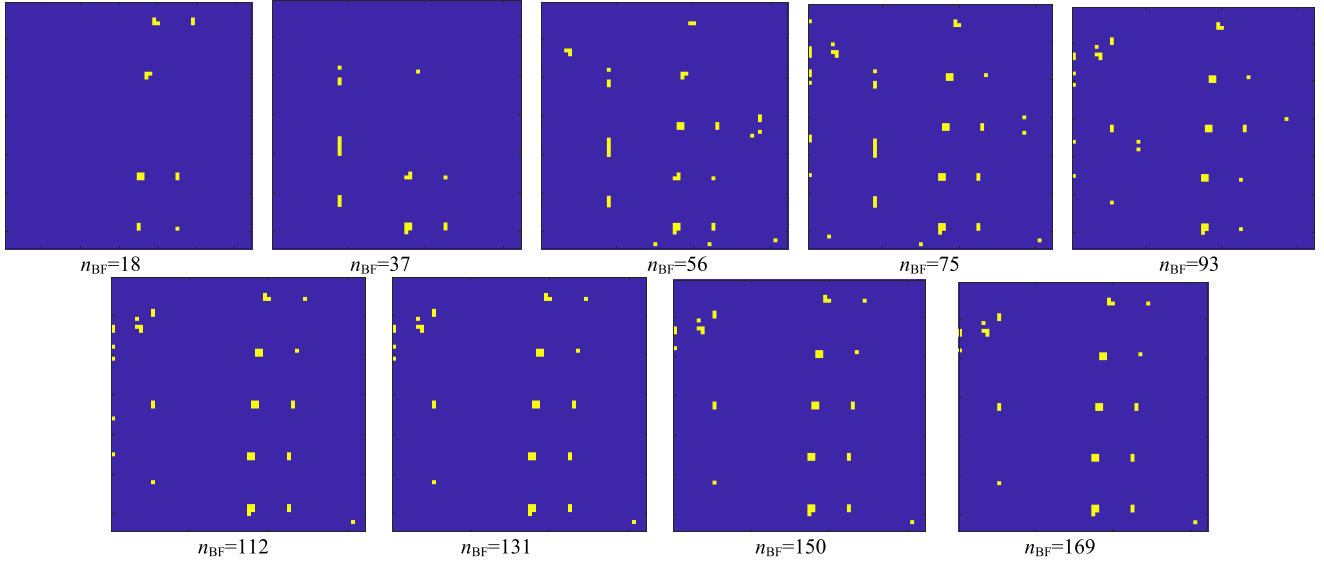


Fig. 14. Binary maps of detection maps in Fig. 13 thresholded by Otsu's method.

TABLE VI
DETECTED ABUNDANCE VALUES OF 19 R PANEL PIXELS OF DIFFERENT SUBSET FUSIONS

Band subsets	1	$1 \cup 2$	$1 \cup 2 \cup 3$	$1 \cup \dots \cup 4$	$1 \cup \dots \cup 5$	$1 \cup \dots \cup 6$	$1 \cup \dots \cup 7$	$1 \cup \dots \cup 8$	$1 \cup \dots \cup 9$
p_{11}	11.1740	41.4735	426.1467	565.6894	803.8325	1365.5095	1496.3245	1524.2666	1534.2729
p_{12}	9.2488	27.7433	150.9704	188.2856	242.9625	467.9701	536.2556	560.6689	594.5325
p_{13}	18.3494	35.5914	57.7685	75.4854	91.2803	169.1479	199.3187	222.3994	244.6013
p_{211}	25.0753	128.4919	245.9841	320.0450	403.5514	485.9469	640.7112	704.2427	733.5450
p_{221}	32.8168	135.6778	249.3081	339.4237	452.6913	531.8716	649.6164	712.1286	733.8726
p_{22}	15.3810	99.6586	173.4740	249.0514	377.5580	452.0189	562.6282	646.1052	717.7250
p_{23}	13.3460	51.3182	68.3732	102.8535	148.4547	199.1693	233.6518	248.6583	295.0736
p_{311}	22.8192	73.9901	717.7234	752.5319	766.9882	806.5271	848.6405	868.9768	887.3359
p_{312}	17.0104	75.5526	825.8751	852.6194	871.8016	933.9430	1006.6296	1021.5325	1042.5020
p_{32}	16.3910	40.8510	339.0274	358.1216	376.5358	391.6702	447.3673	470.0582	488.6069
p_{33}	17.7917	44.8807	166.9810	181.5010	194.4998	218.2995	239.8715	271.2274	301.2609
p_{411}	38.7299	237.4271	262.4541	483.9900	601.0014	783.5891	876.3403	1001.3679	1079.1877
p_{412}	55.8119	344.7630	388.9848	566.4575	651.8406	757.6087	870.5034	937.6919	1006.1327
p_{42}	35.7348	188.1820	212.0321	390.8717	456.8636	554.5633	667.2411	745.1382	789.8681
p_{43}	16.5454	36.3748	49.0050	133.5310	151.0750	186.3171	224.1015	237.2814	287.5233
p_{511}	37.7443	393.2389	434.9214	478.6209	521.7614	572.1187	661.7849	697.1774	732.7601
p_{521}	118.6343	709.8326	747.8079	829.6747	937.2388	1009.4289	1116.0018	1150.3468	1192.3064
p_{52}	64.4979	423.6777	448.5125	513.3513	570.5321	705.1881	798.1036	841.0248	858.3700
p_{53}	19.2434	59.7609	67.4249	126.2885	143.3660	168.9125	196.2244	216.1771	240.7273

As shown in Figs. 8 and 9, fusing only three-band subsets Bsubsets ($1 \cup 19 \cup 2$) already produced very good AD results where most anomalies were detected, and background was sufficiently suppressed. The detection results were then stable after a second fusion process of fusing a third band subset by PBSF. Then, the fusion of subsequent band subsets did not have much impact on the detection results afterward. To further conduct quantitative analysis, Fig. 10 plots the 3-D ROC curves of the anomaly abundance detection maps in Fig. 8 along with their corresponding three 2-D ROC curves. Table IV tabulates the AUC values calculated from the eight detection measures in Section V where the best results are boldfaced. From Table IV, if we solely rely on the $AUC_{(D,F)}$ values, the best result was 0.9899 produced by fusing $((1 \cup 19) \cup \dots \cup 12) \cup 9$. However, if we further compare seven other detection measures, the best result was actually the one after the first fusion process, i.e., $1 \cup 19$, which yielded the

best results across the board except for $AUC_{(D,F)}$, which was 0.9837 slightly worse than 0.9899. This indicated that PBSF of UBS could be very effective by fusing only two UBS band subsets, and using full bands was not necessary to produce the best results. Similar conclusions can be also drawn for the other four scenarios.

VII. INTERBAND SUBSETS IMPLEMENTED BY PBSF

In Section III-A, we only describe how PBSF fuses the MBS band subset-by-band subset progressively. However, the issue of how to fuse individual bands in different band subsets is not addressed. In what follows, we describe three different ways to fuse individual bands in two separate band subsets.

A. Progressive Band Fusion-BSQ

Since PBSF-BSQ performs the BSQ format, nine Bsubsets to be fused must be consecutive, as tabulated in Table V,

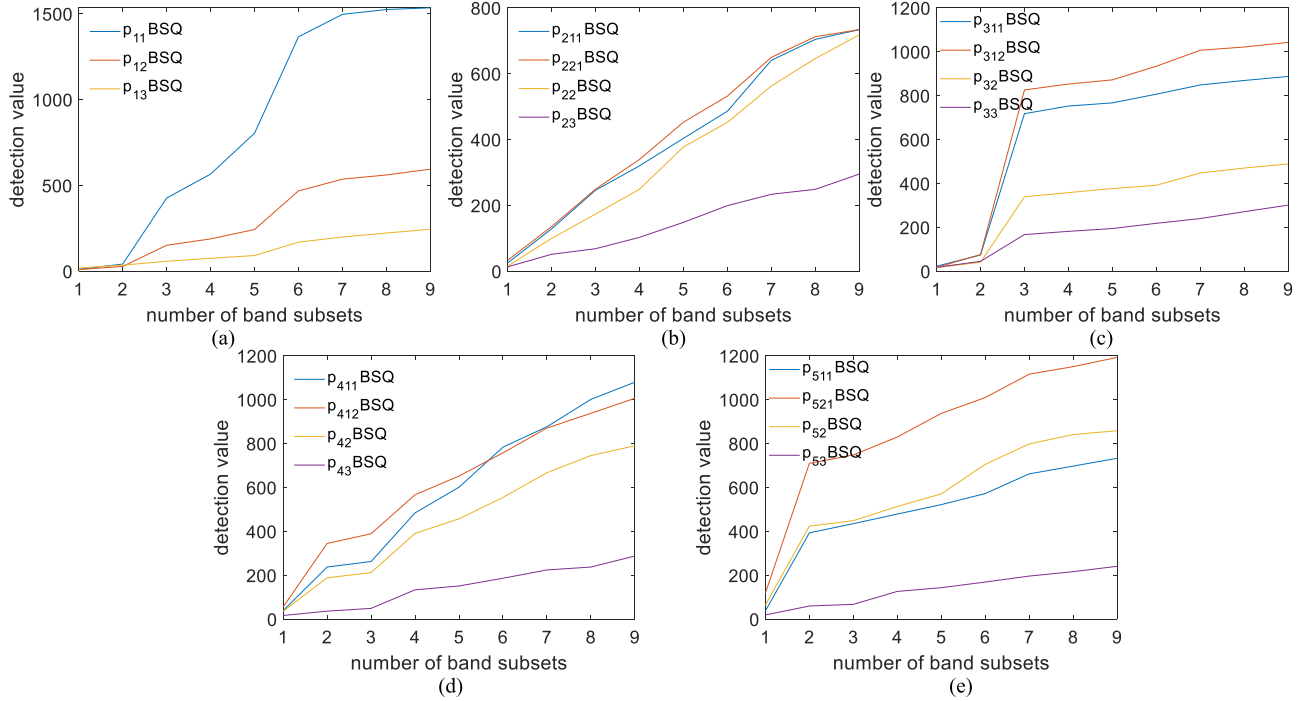


Fig. 15. Detected abundance values of 19 R panel pixels as the number of band subsets is increased. (a) Detection of R panel pixels in row 1. (b) Detection of R panel pixels in row 2. (c) Detection of R panel pixels in row 3. (d) Detection of R panel pixels in row 4. (e) Detection of R panel pixels in row 5.

TABLE VII
BAND SUBSETS FOR PBSF-RT FOR HYDICE DATA IN FIG. 4

	Station 1	Station 2	Station 3	Station 4	Station 5	Station 6	Station 7	Station 8	Station 9
Bsubset 1	1	19	38	57	76	94	113	132	151
Bsubset 2	2	20	39	58	77	95	114	133	152
Bsubset 3	3	21	40	59	78	96	115	134	153
Bsubset 4	4	22	41	60	79	97	116	135	154
Bsubset 5	5	23	42	61	80	98	117	136	155
Bsubset 6	6	24	43	62	81	99	118	137	156
Bsubset 7	7	25	44	63	82	100	119	138	157
Bsubset 8	8	26	45	64	83	101	120	139	158
Bsubset 9	9	27	46	65	84	102	121	140	159
Bsubset 10	10	28	47	66	85	103	122	141	160
Bsubset 11	11	29	48	67	86	104	123	142	161
Bsubset 12	12	30	49	68	87	105	124	143	162
Bsubset 13	13	31	50	69	88	106	125	144	163
Bsubset 14	14	32	51	70	89	107	126	145	164
Bsubset 15	15	33	52	71	90	108	127	146	165
Bsubset 16	16	34	53	72	91	109	128	147	166
Bsubset 17	17	35	54	73	92	110	129	148	167
Bsubset 18	18	36	55	74	93	111	130	149	168

with Bsubset1: 1 \cup 2 \cup ... \cup 18, Bsubset 2: 19 \cup 20 \cup ... \cup 37, ..., Bsubset 9: 151 \cup 152 \cup ... \cup 169, in which case each receiving station fuses one Bsubset simultaneously by BSQ in parallel. Fig. 11 shows the R-AD detected anomaly abundance maps of nine Bsubsets received and processed by each of nine receiving stations individually and simultaneously along with Fig. 12, which shows their corresponding binary maps obtained by Otsu's method. It should be noted that the number of bands used by each receiving station was the same, but the detection results in Figs. 11 and 12 show that different band subsets yielded different detection capabilities. For example, station7 detected most of the panel pixels in Fig. 11, which

confirmed the results in Figs. 4 and 5, where using \mathbf{B}_{SWIR} produced good results. By contrast, station5 detected almost nothing except two anomalous pixels at the upper left corner, which were rocks in Fig. 11.

The results in Fig. 11 illustrated that using PBSF-BSQ was not effective, and MBS fusion was needed. Fig. 13 shows their progressively fused detection results obtained by PBSF-MBS, which fused Bsubset1 \cup Bsubset2 \cup ... \cup Bsubset9 with the number of bands being fused, (n_{BF}) specified underneath each figure. For example, fusing the first three-band subsets, Bsubset1 \cup Bsubset2 \cup Bsubset3 with $n_{\text{BF}} = 56$ showed a large change in detection results, and then, the

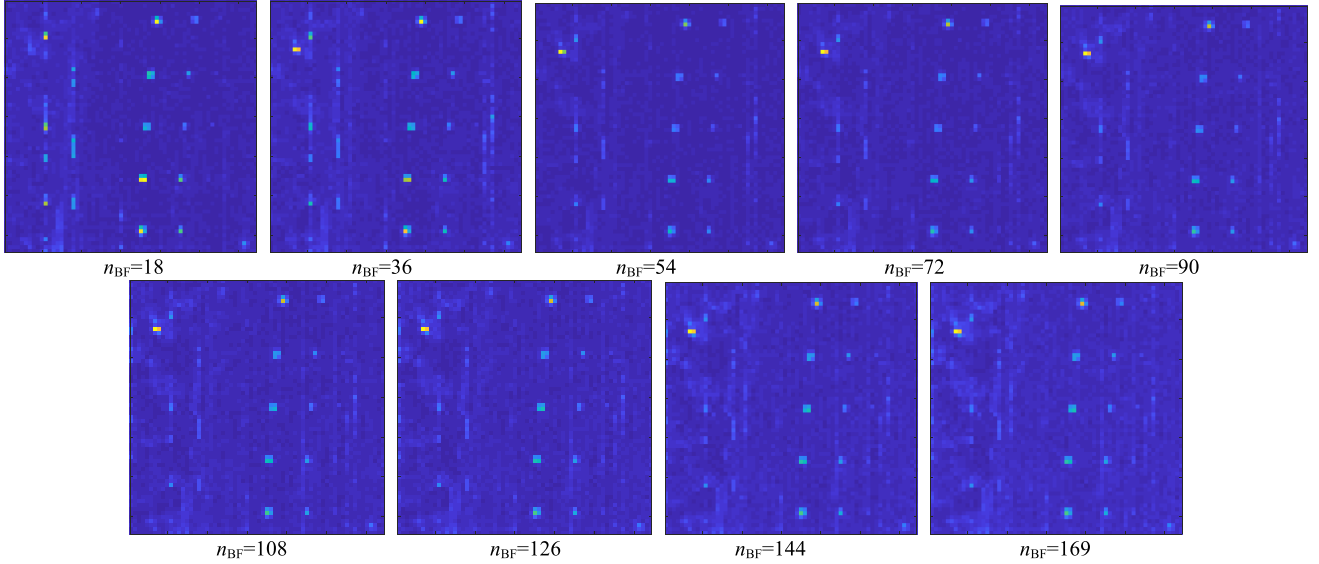


Fig. 16. R-AD detection maps of using PBSF-RT.

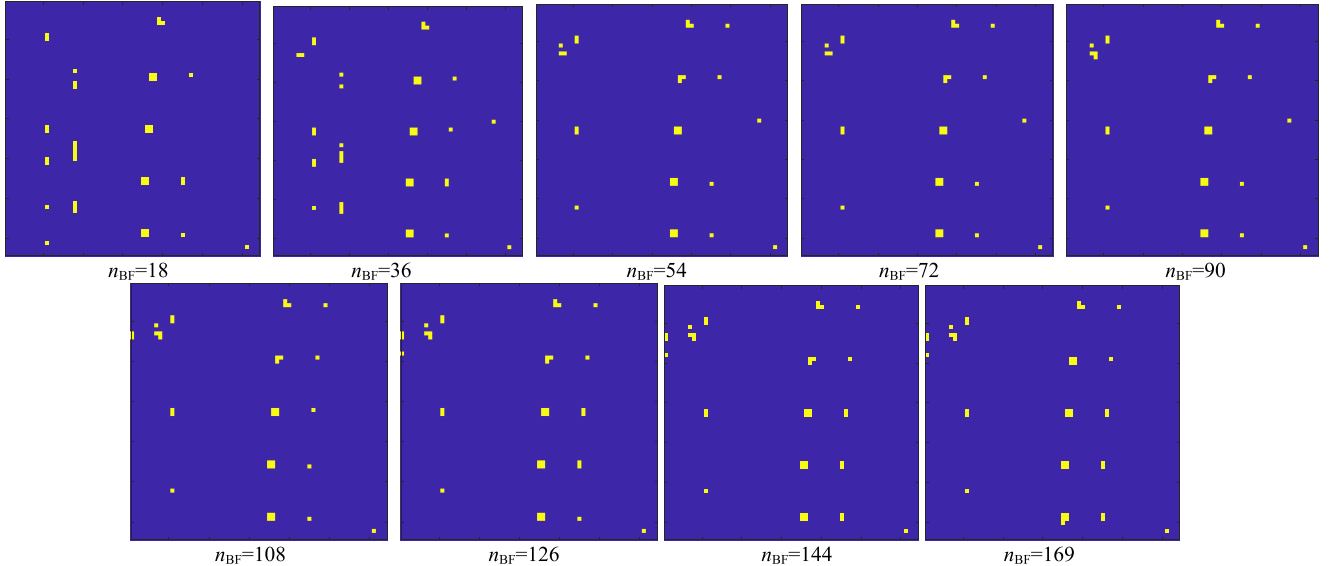


Fig. 17. Binary maps of Fig. 16 thresholded by Otsu's method.

detection performance was slightly improved until it reached $B_{\text{subset}1} \cup B_{\text{subset}2} \cup \dots \cup B_{\text{subset}6}$ with $n_{\text{BF}} = 112$ where the detection performance became stable afterward. When all bands were fused with $n_{\text{BF}} = 169$, the fusion result was identical to that obtained by using all bands simultaneously for detection. Fig. 14 also shows the binary maps obtained from Fig. 13 by Otsu's method, and Table VI tabulates the detected abundance values of 19 R panel pixels in the fusion process, which are plotted in Fig. 15, as the number of band subsets is increased.

The results in Table VI and Fig. 13 show that the more the band subsets were fused, the greater the detected values were for all 19 R panel pixels. In the PBSF-BSQ, the bands to be processed were distributed to different receiving stations where each receiving station processed the data in parallel to produce their own detection results, and then, their results were further

fused station by station. The disadvantage of PBSF-BSQ is that the fusion process must follow the BSQ format band by band consecutively.

B. Progressive Band Subset Fusion in Real Time

This experiment is designed to illustrate PBSF-RT which is actually scenario 1 discussed in PBSF of UBS in Section III-B where each receiving station receives bands in parallel, and then, these received bands will form a band subset for RT-AD every time a band is received. The 169 bands of HYDICE data were distributed to nine receiving stations, which processed band subsets in parallel, as tabulated in Table VII. For example, each receiving station receives its first band in its own designated band subset, and then, the first bands were fused by SBF to produce detection results, denoted by $B_{\text{subset}1}$. After the first bands in all band subsets were processed

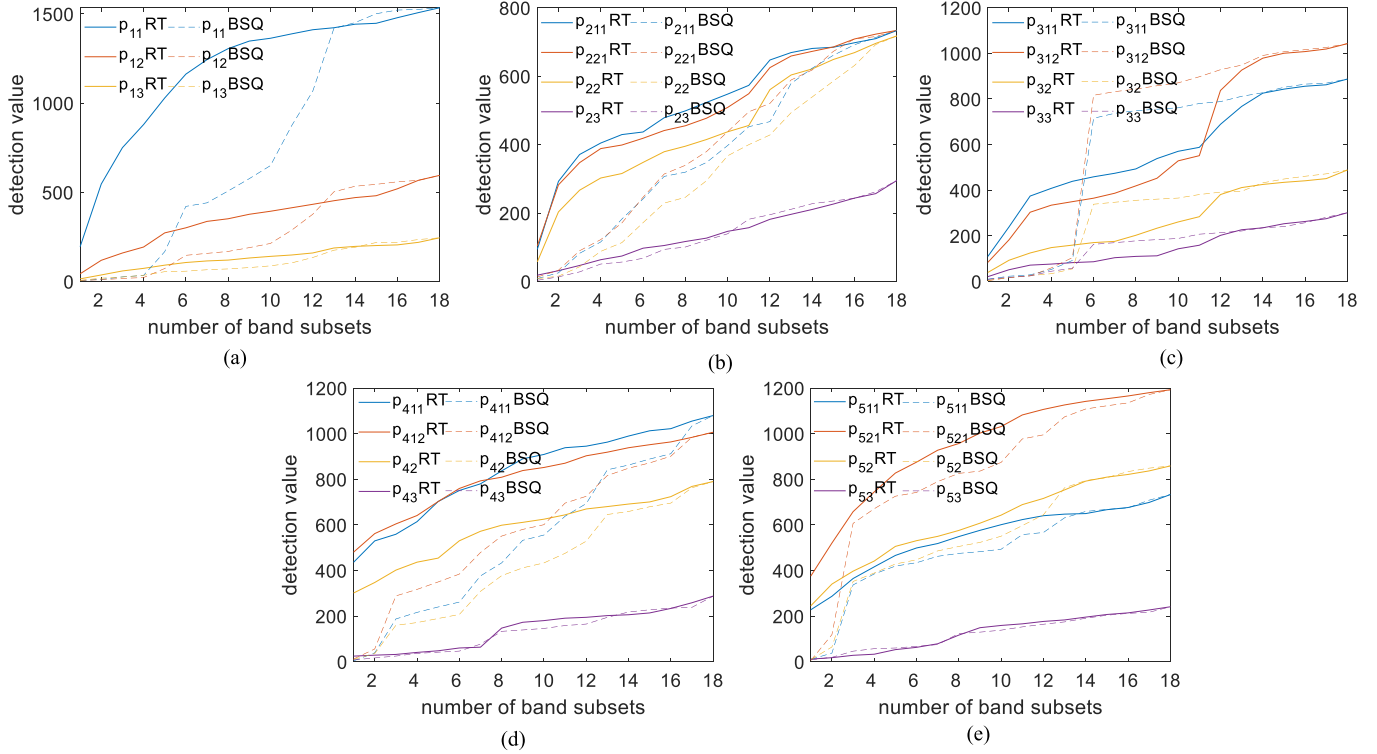


Fig. 18. Detected abundance values of 19 R panel pixels using PBSF-BSQ and PBSF-RT. (a) Detection of R panel pixels in row 1. (b) Detection of R panel pixels in row 2. (c) Detection of R panel pixels in row 3. (d) Detection of R panel pixels in row 4. (e) Detection of R panel pixels in row 5.

simultaneously, the second band received by all receiving stations in their own band subsets were also in process and fused by SBF with Bsubset1 to produce detection results, denoted by Bsubset2. The same process was repeated until all 169 bands were fused. It is worth noting that three processes, the transmission of bands, the detection of anomalies, and the fusion of band subsets, were carried out simultaneously in RT. Fig. 16 shows the abundance changes in R-AD detection maps during the fusion process of PBSF-RT, which not only detected anomalies on a timely basis but also suppressed the background as well. To further see quantitative detection results in Fig. 16, Otsu's method was used to threshold the detection maps in Fig. 16 to produce their respective binary maps in Fig. 17.

As shown in Figs. 16 and 17, most anomalies were detected at the initial stage of PBSF-RT. The anomaly abundance detection maps of the fusion process were improved steadily as more bands were fused. Fig. 18 shows the detected abundance values of 19 R panel pixels using PBSF-BSQ and PBSF-RT where the plots generated by PBSF-BSQ and PBSF-RT are marked by dotted lines and solid lines, respectively.

Comparing PBSF-RT to PBSF-BSQ, the detected abundance values of 19 R panels by PBSF-RT after initial fusion were greater than PBSF-BSQ. Also, when the same number of bands were fused, the detected abundance values of panels by PBSF-RT were generally greater than that detected by PBSF-BSQ. This indicated that PBSF-RT could detect more anomalies by fusing fewer bands. The last but not least, PBSF-RT can be implemented in RT detection, while PBSF-BSQ could not but rather be implemented progressively.

TABLE VIII
DETECTION VALUES OF 19 R PANEL PIXELS

panel pixel	Detection values		
	PBSF-BSQ	PBSF-RT	PBSF-zigzag1/2
p ₁₁	11.17	546.20	274.70
p ₁₂	9.25	118.50	57.34
p ₁₃	18.35	36.30	28.46
p ₂₁₁	25.08	292.50	141.40
p ₂₂₁	32.82	282.30	160.60
p ₂₂	15.38	203.20	89.23
p ₂₃	13.35	31.39	29.66
p ₃₁₁	22.82	238.90	168.20
p ₃₁₂	17.01	182.40	130.60
p ₃₂	16.39	92.85	61.25
p ₃₃	17.79	51.27	37.47
p ₄₁₁	38.73	529.70	464.10
p ₄₁₂	55.81	561.70	506.40
p ₄₂	35.73	347.20	315.30
p ₄₃	16.55	28.64	28.59
p ₅₁₁	37.74	286.90	302.90
p ₅₂₁	118.63	520.30	589.30
p ₅₂	64.50	340.40	354.00
p ₅₃	19.24	17.57	21.45

C. Progressive Band Fusion-Zigzag (PBSF-ZIGZAG)

This section performed experiments by fusing band subsets in a zig-zag manner. Two PBSF-zigzag methods, PBSF-zigzag1 and PBSF-zigzag2 introduced in Section IV-C, were implemented to detect anomalies of HYDICE, respectively. Fig. 19 shows the detected abundance values of 19 R panel pixels using PBSF-BSQ and two PBSF-zigzag methods

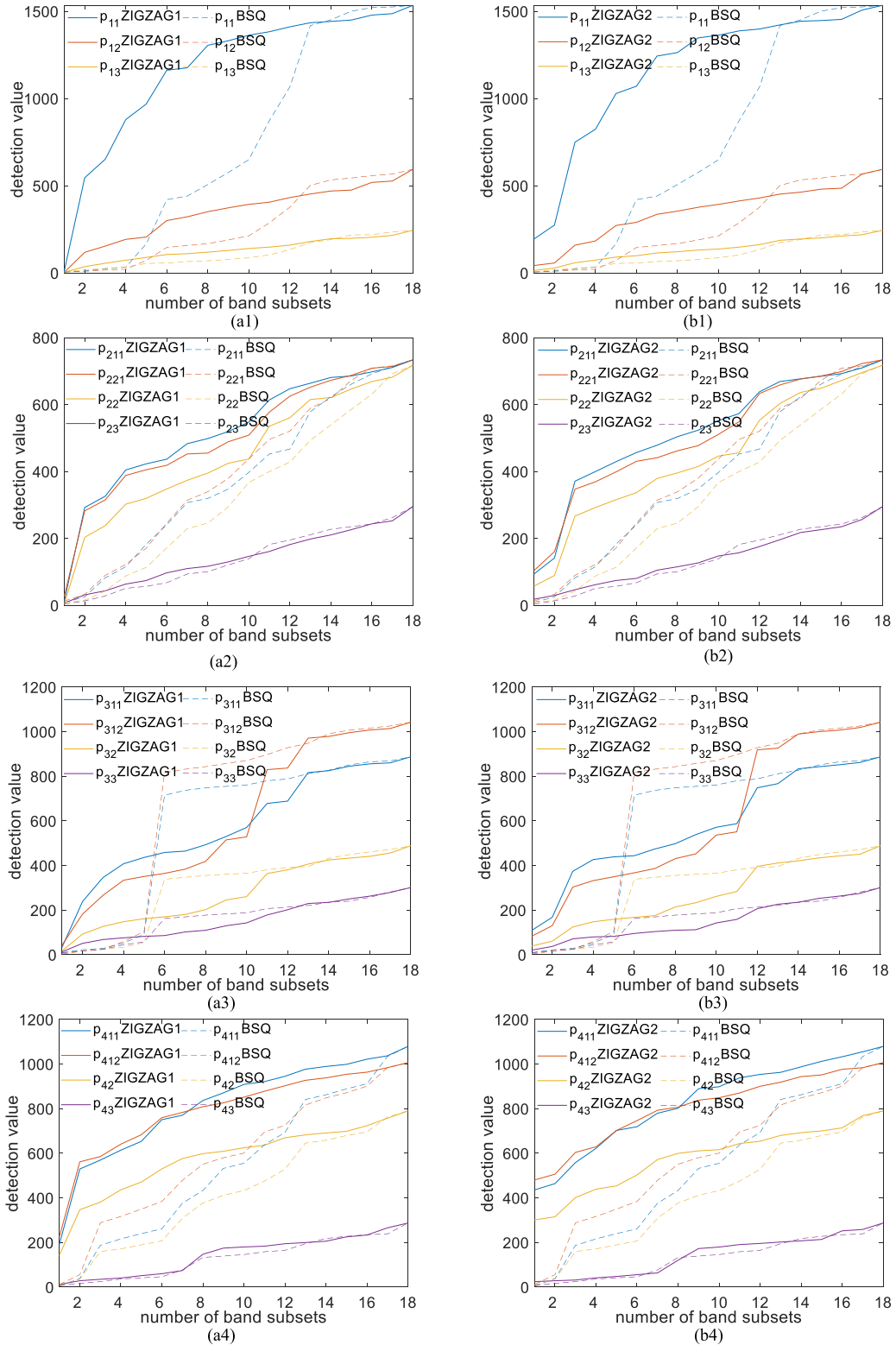


Fig. 19. Detection value fractions of 19 R panel pixels using PBSF-BSQ and PBSF-zigzag. (a1) detection of R panel pixels in row 1. (a2) Detection of R panel pixels in row 2. (a3) Detection of R panel pixels in row 3. (a4) Detection of R panel pixels in row 4. (a5) Detection of R panel pixels in row 5, PBSF-zigzag1. (b1) Detection of R panel pixels in row 1. (b2) Detection of R panel pixels in row 2. (b3) Detection of R panel pixels in row 3. (b4) Detection of R panel pixels in row 5, PBSF-zigzag2.

where the plots by PBSF-BSQ and PBSF-zigzag are marked by dotted lines and solid lines, respectively.

Similar to PBSF-RT, PBSF-zigzag1 and PBSF-zigzag2, denoted by PBSF-zigzag1/2, also produced greater abundance

values in their initial fusions. In addition, PBSF-zigzag1/2 detected more panel pixels fusing fewer bands than PBSF-RT. To conduct quantitative analysis, the detected abundance values of all 19 R panel pixels were tabulated in Table VIII for

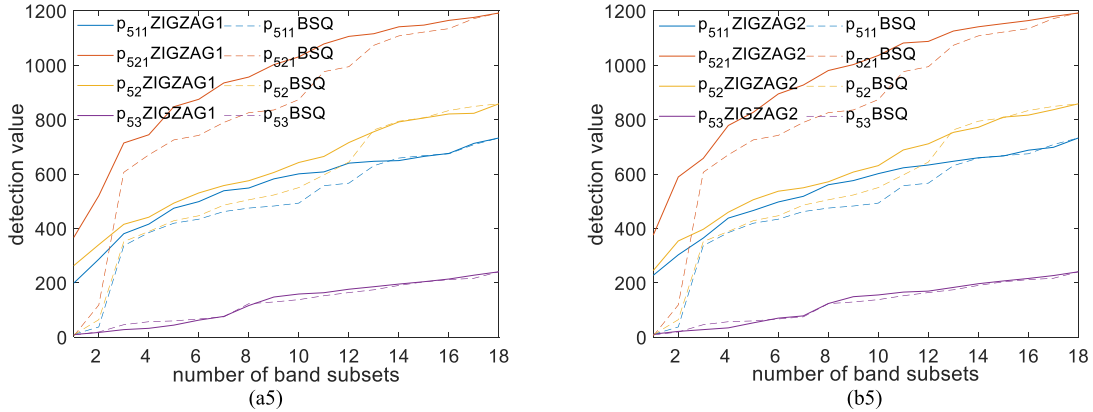


Fig. 19. (Continued.) Detection value fractions of 19 R panel pixels using PBSF-BSQ and PBSF-zigzag. (a1) detection of R panel pixels in row 1. (a2) Detection of R panel pixels in row 2. (a3) Detection of R panel pixels in row 3. (a4) Detection of R panel pixels in row 4. (a5) Detection of R panel pixels in row 5, PBSF-zigzag1. (b1) Detection of R panel pixels in row 1. (b2) Detection of R panel pixels in row 2. (b3) Detection of R panel pixels in row 3. (b4) Detection of R panel pixels in row 4. (b5) Detection of R panel pixels in row 5, PBSF-zigzag2.

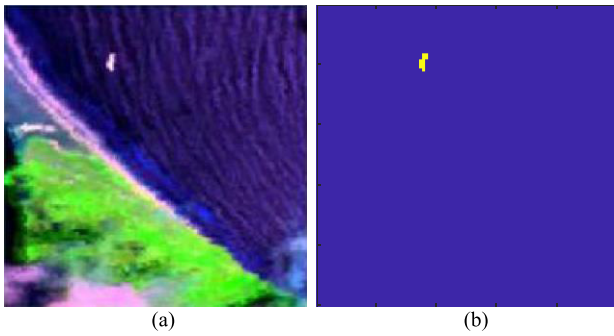


Fig. 20. (a) AVIRIS scene. (b) Ground-truth map of spatial locations of ten anomalous pixels.

PBSF-BSQ, PBSF-RT, and PBSF-zigzag1/2 where the best results are boldfaced. As shown in Table VIII, PBSF-RT did the best for all panel pixels in rows 1–4 except for the panel pixels in row 5 for which PBSF-zigzag1/2 did the best.

VIII. AVIRIS IMAGE EXPERIMENTS FOR PBSF-MBS AND PBSF-UBS

A second dataset was for experiments. It is an airborne visible/infrared imaging spectrometer (AVIRIS) sensor collected over the Bay Champagne area in April 2010 [37]. The image has a size of $100 \times 100 \times 188$ pixels with noisy bands removed. The spatial resolution of the image is 4.4 m. The ground truth of this dataset includes ten anomalous pixels. The sample image and reference detection map for this dataset are shown in Fig. 20(a) and (b), respectively.

Since similar conclusions drawn for HYDICE data in Fig. 4 are also applicable to the AVIRIS dataset, only experiments similar to that designed for PBSF-MBS and PBSF-UBS for HYDICE data were also conducted for this dataset.

A. PBSF-MBS

In analogy with Section VI-A, we also divide this range into three regions of interest: the visible range from 400 to 750 nm, the NIR range from 750 to 1400 nm, and the SWIR range

from 1400 to 2500 nm. Let these three-band subsets be denoted by \mathbf{B}_{VIS} , \mathbf{B}_{NIR} , and \mathbf{B}_{SWIR} with their bands tabulated in Table IX, which are assumed to be transmitted to three different receiving stations. Fig. 21 shows the detected anomaly abundance maps by R-AD using single-band subset \mathbf{B}_{VIS} , \mathbf{B}_{NIR} , and \mathbf{B}_{SWIR} , fusing three-band subsets, $\mathbf{B}_{\text{VIS}} \cup \mathbf{B}_{\text{NIR}}$, $\mathbf{B}_{\text{VIS}} \cup \mathbf{B}_{\text{SWIR}}$, and $\mathbf{B}_{\text{NIR}} \cup \mathbf{B}_{\text{SWIR}}$, and also fusing three-band subsets, $(\mathbf{B}_{\text{VIS}} \cup \mathbf{B}_{\text{NIR}}) \cup \mathbf{B}_{\text{SWIR}}$, $(\mathbf{B}_{\text{VIS}} \cup \mathbf{B}_{\text{SWIR}}) \cup \mathbf{B}_{\text{NIR}}$, and $(\mathbf{B}_{\text{NIR}} \cup \mathbf{B}_{\text{SWIR}}) \cup \mathbf{B}_{\text{VIS}}$. Based on visual inspection, all the detection results in Fig. 21 were very close where the anomalies were detected and the background was also well suppressed. In this case, Otsu's method was used to threshold the anomaly abundance maps in Fig. 21, and Fig. 22 shows their corresponding binary AD maps where the best results were obtained by \mathbf{B}_{SWIR} , $\mathbf{B}_{\text{VIS}} \cup \mathbf{B}_{\text{SWIR}}$, $(\mathbf{B}_{\text{VIS}} \cup \mathbf{B}_{\text{NIR}}) \cup \mathbf{B}_{\text{SWIR}}$, $(\mathbf{B}_{\text{VIS}} \cup \mathbf{B}_{\text{SWIR}}) \cup \mathbf{B}_{\text{NIR}}$, and $(\mathbf{B}_{\text{NIR}} \cup \mathbf{B}_{\text{SWIR}}) \cup \mathbf{B}_{\text{VIS}}$.

To conduct detailed quantitative studies, Fig. 23 plots 3-D ROC curves along with their corresponding three 2-D ROC curves. Table X tabulates AUC values calculated by eight detection measures introduced in Section V where the best results are boldfaced. Specifically, $\mathbf{B}_{\text{NIR}} \cup \mathbf{B}_{\text{SWIR}}$ and $(\mathbf{B}_{\text{VIS}} \cup \mathbf{B}_{\text{NIR}}) \cup \mathbf{B}_{\text{SWIR}}$ produced the highest value of $\text{AUC}_{(D,F)}$ to evaluate the effectiveness of AD. On the other hand, $\mathbf{B}_{\text{VIS}} \cup \mathbf{B}_{\text{NIR}}$ produced the highest value of $\text{AUC}_{(D,t)}$ to show the best TD of anomalies as opposed to \mathbf{B}_{SWIR} that produced the lowest value of $\text{AUC}_{(F,t)}$ to reflect the best BS for AD. Nevertheless, overall speaking, the best result was produced by $\mathbf{B}_{\text{VIS}} \cup \mathbf{B}_{\text{NIR}}$, which has the best values among four out of eight detection measures.

However, if we further examine the thresholded binary maps in Fig. 22, $\mathbf{B}_{\text{VIS}} \cup \mathbf{B}_{\text{NIR}}$ was among the four worst results but was one of the best results in abundance AD maps in Fig. 21. This intriguing scenario demonstrated an important fact that relying on single-thresholded binary maps, such as Otsu's method, is not reliable where Otsu's threshold method is a widely used technique in image thresholding [38] but not necessary to be optimal [39]. This also explains why 3-D ROC curve-derived detection measures are needed. For example, a common practice to conduct a comparative performance

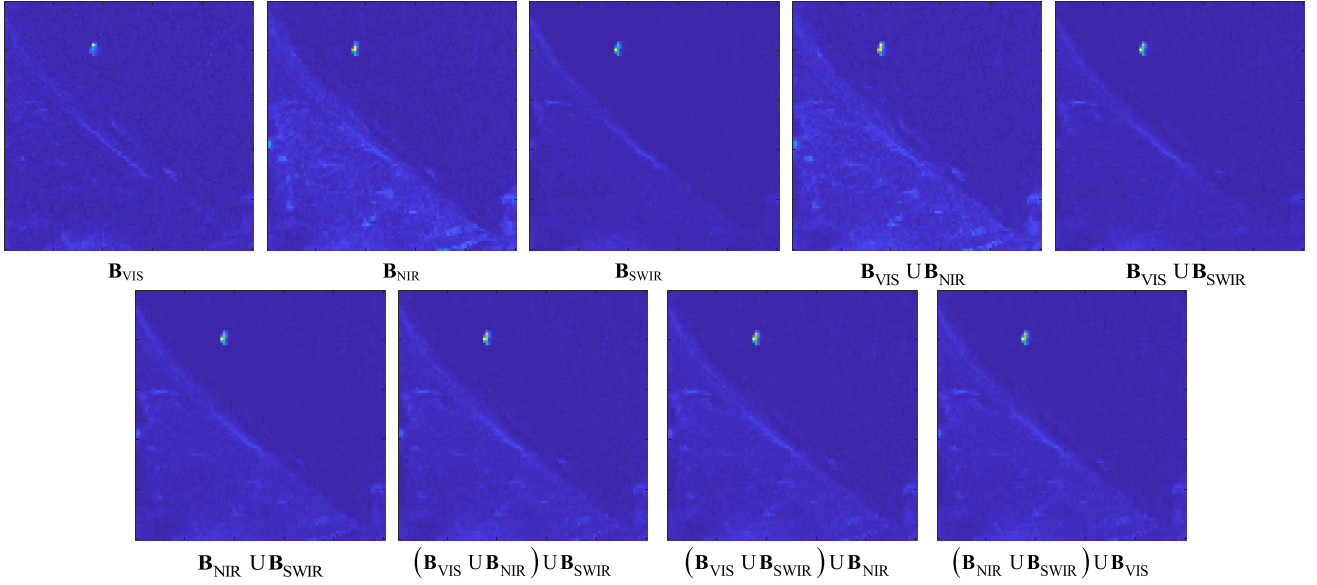


Fig. 21. R-AD detected anomaly maps of different BF sets.

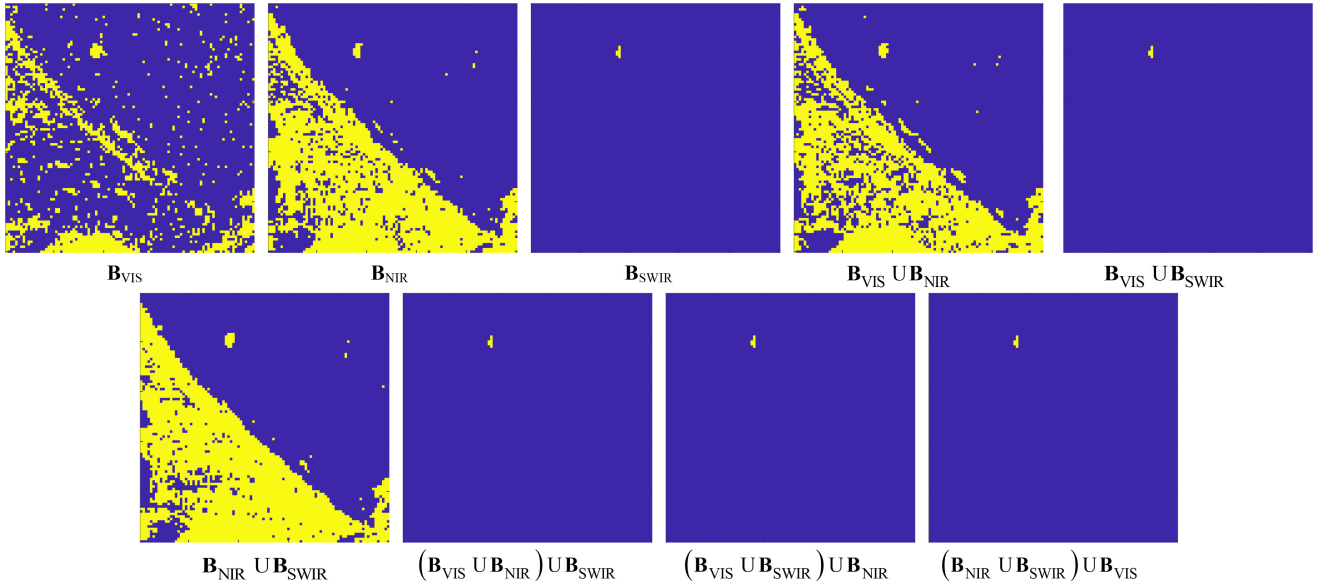


Fig. 22. Binary maps of different BF sets thresholded by Otsu's method.

TABLE IX
BAND SUBSETS SELECTED FOR VIS, NIR, AND SWIR SPECTRAL RANGES FOR AVIRIS DATA IN FIG. 20

Receiving station	Bsubset	Spectral wavelength(nm)	Spectral band
1	\mathbf{B}_{VIS}	400-750	1-32
2	\mathbf{B}_{NIR}	750-1400	33-96
3	\mathbf{B}_{SWIR}	140-25000	97-188

analysis is evaluated based on the value of P_D with a fixed value or based on the value of P_F by fixing P_D at a certain value, such as experiments in [40, Tables II and III and Figs. 10–15]. However, it was shown in [41] that such an approach may, unfortunately, mislead conclusions. To resolve this dilemma, the 3-D ROC analysis has been recently used for the performance evaluation of AD [21]–[23], [41]–[44].

B. PBSF-UBS

To implement PBSF-UBS, we need to estimate VD for the AVIRIS scene in Fig. 20, which is $n_{\text{VD}} = 13$ by HFC [34]. Accordingly, $n_{\text{VD}} = 13$ was used to determine 13-band subsets to be fused by PBSF-UBS for experiments. In this case, we can assume that the 188 bands of AVIRIS are divided into 13-band subsets and transmitted to the corresponding

TABLE X

VARIOUS AUC VALUES CALCULATED FROM THE THREE 2-D ROC CURVES OF DETECTION RESULTS IN FIG. 23 USING DIFFERENT BAND SUBSETS

Band subsets	AUC _(D,F)	AUC _(D,τ)	AUC _(F,τ)	AUC _{TD}	AUC _{BS}	AUC _{TDBS}	AUC _{COPD}	AUC _{SNPR}
B_{VIS}	0.9950	0.2832	0.0253	1.2782	0.9697	0.2579	1.2529	11.1850
B_{NIR}	0.9963	0.4332	0.0366	1.4294	0.9596	0.3965	1.3928	11.8210
B_{SWIR}	0.9996	0.3795	0.0171	1.3791	0.9825	0.3625	1.3620	22.2034
B_{VIS} UB_{NIR}	0.9979	0.5259	0.0392	1.5238	0.9587	0.4867	1.4846	13.4113
B_{VIS} UB_{SWIR}	0.9996	0.4486	0.0214	1.4483	0.9782	0.4272	1.4269	20.9418
B_{NIR} UB_{SWIR}	0.9997	0.4486	0.0239	1.4483	0.9758	0.4247	1.4244	18.7667
B_{VIS} UB_{NIR} UB_{SWIR}	0.9997	0.4886	0.0257	1.4884	0.9740	0.4629	1.4627	19.0190

TABLE XI

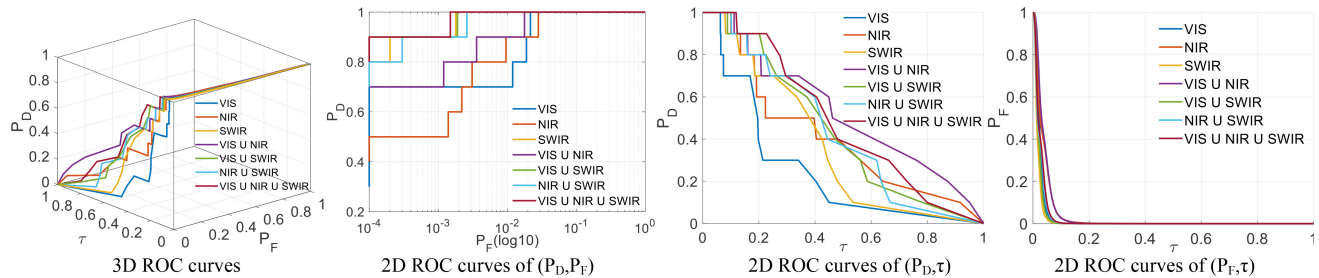
BAND SUBSETS SELECTED FOR PBSF-UBS FOR AVIRIS DATA IN FIG. 20

Receiving stations	Bsubsets												
	1	15	29	44	58	73	87	102	116	131	145	160	174
2	2	16	30	45	59	74	88	103	117	132	146	161	175
3	3	17	31	46	60	75	89	104	118	133	147	162	176
4	4	18	32	47	61	76	90	105	119	134	148	163	177
5	5	19	33	48	62	77	91	106	120	135	149	164	178
6	6	20	34	49	63	78	92	107	121	136	150	165	179
7	7	21	35	50	64	79	93	108	122	137	151	166	180
8	8	22	36	51	65	80	94	109	123	138	152	167	181
9	9	23	37	52	66	81	95	110	124	139	153	168	182
10	10	24	38	53	67	82	96	111	125	140	154	169	183
11	11	25	39	54	68	83	97	112	126	141	155	170	184
12	12	26	40	55	69	84	98	113	127	142	156	171	185
13	13	27	41	56	70	85	99	114	128	143	157	172	186
14	14	28	42	57	71	86	100	115	129	144	158	173	187
15			43		72		101		130		159		188

TABLE XII

VARIOUS AUC VALUES CALCULATED FROM THE THREE 2-D ROC CURVES OF DETECTION RESULTS IN FIG. 26 USING DIFFERENT BAND SUBSETS

Band subsets	AUC _(D,F)	AUC _(D,τ)	AUC _(F,τ)	AUC _{TD}	AUC _{BS}	AUC _{TDBS}	AUC _{COPD}	AUC _{SNPR}
1 U 15	0.9997	0.4486	0.0156	1.4484	0.9841	0.4330	1.4328	28.7477
(1 U 15) U 2	0.9997	0.4968	0.0215	1.4965	0.9781	0.4753	1.4749	23.0692
((1 U 15) U 2) U 14	0.9997	0.5114	0.0236	1.5110	0.9761	0.4878	1.4874	21.6836
((1 U 15) U ... U 14) U 3	0.9998	0.4823	0.0214	1.4820	0.9783	0.4609	1.4606	22.5203
((1 U 15) U ... U 3) U 13	0.9996	0.4959	0.0239	1.4955	0.9757	0.4720	1.4716	20.7598
((1 U 15) U ... U 13) U 4	0.9996	0.4777	0.0212	1.4774	0.9784	0.4565	1.4561	22.4961
((1 U 15) U ... U 4) U 12	0.9997	0.4814	0.0237	1.4811	0.9761	0.4577	1.4574	20.3425
((1 U 15) U ... U 12) U 5	0.9997	0.4614	0.0225	1.4611	0.9772	0.4389	1.4386	20.5078
((1 U 15) U ... U 5) U 11	0.9997	0.4768	0.0235	1.4765	0.9761	0.4533	1.4530	20.2522
((1 U 15) U ... U 11) U 6	0.9998	0.4768	0.0240	1.4766	0.9757	0.4528	1.4525	19.8269
((1 U 15) U ... U 6) U 10	0.9998	0.4841	0.0247	1.4838	0.9750	0.4594	1.4591	19.5838
((1 U 15) U ... U 10) U 7	0.9997	0.4850	0.0264	1.4847	0.9734	0.4586	1.4584	18.3879
((1 U 15) U ... U 7) U 9	0.9997	0.4886	0.0252	1.4884	0.9745	0.4634	1.4631	19.3642
((1 U 15) U ... U 9) U 8	0.9997	0.4886	0.0257	1.4884	0.9740	0.4629	1.4627	19.0190

Fig. 23. 3-D ROC curves along with their generated three 2-D ROC curves of R-AD detected anomaly maps of **B_{VIS}**, **B_{NIR}**, **B_{SWIR}**, **B_{VIS} U B_{NIR}**, **B_{VIS} U B_{SWIR}**, **B_{NIR} U B_{SWIR}**, and **(B_{VIS} U B_{NIR}) U B_{SWIR}**.

13 receiving stations, each of which will receive 14 or 15 bands simultaneously. When $n_{BS} = 13$, $\lceil 188/13 \rceil = 15$, and the last one band subset has only six bands. In this case,

there are 15 receiving stations that are collected synchronously beginning with different initial conditions. Except for the last 15th station receiving six bands, all other 14 receiving stations

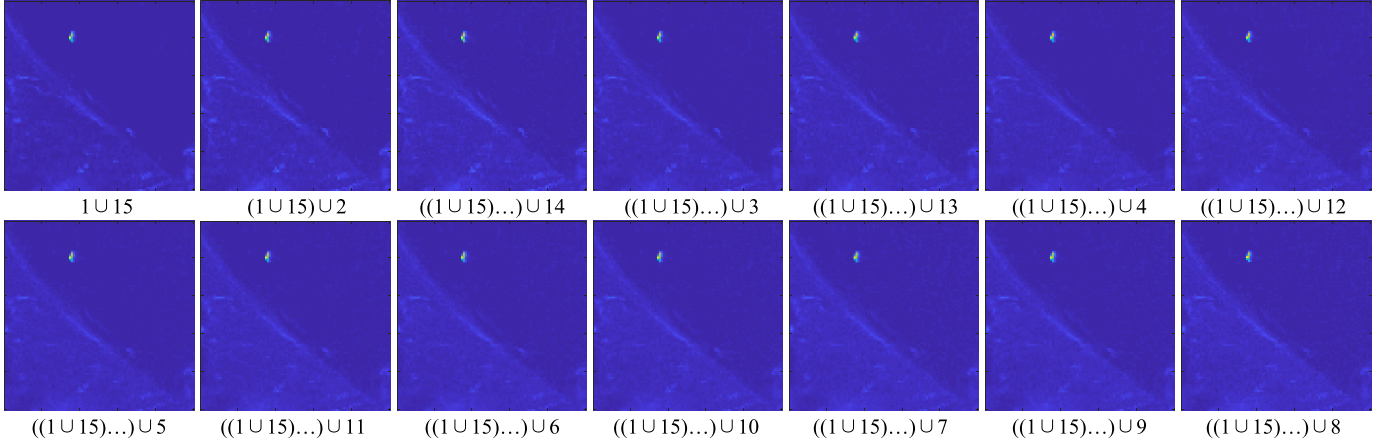


Fig. 24. R-AD detected anomaly maps of different BF subsets.

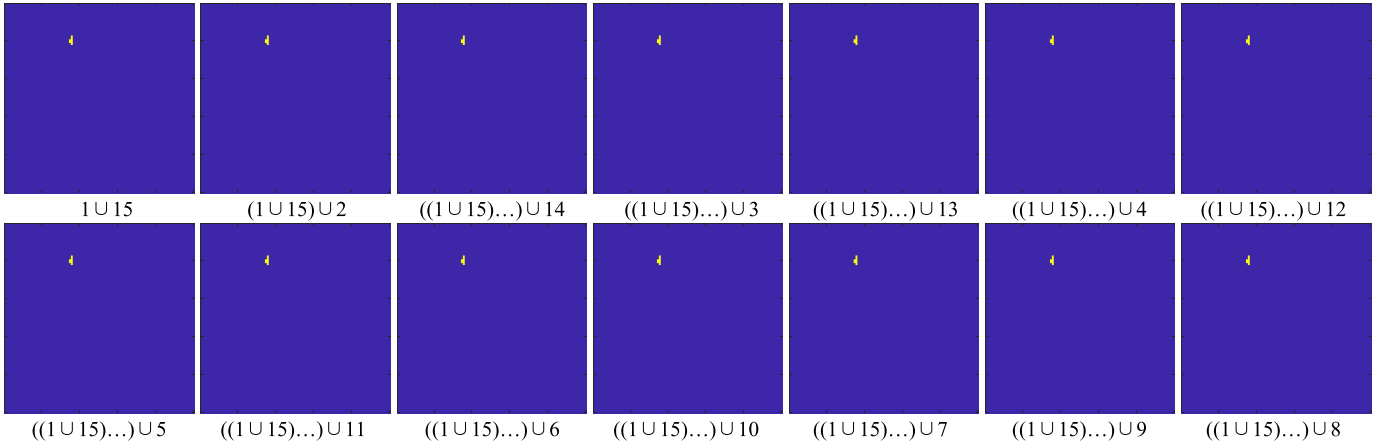


Fig. 25. Binary maps of different BF subsets by Otsu's method.

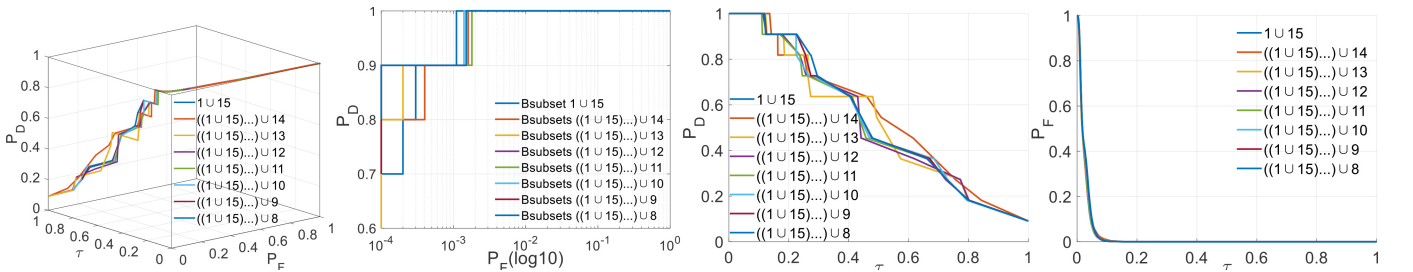


Fig. 26. 3-D ROC curves along with their generated three 2-D ROC curves of R-AD detected anomaly maps in Fig. 24 by fusing different subsets.

will receive 13 bands. Since $\lceil 15/2 \rceil = 8$, the fusion will be terminated at the eight-band subset, Bsubset8. Table XI tabulates the bands in each of 13-band subsets according to different bands used to initialize UBS except the last receiving station that receives only six bands. Fig. 24 shows the anomaly abundance detection maps of PBSF implemented by R-AD along with their Otsu's thresholded binary maps shown in Fig. 25.

As shown in Figs. 24 and 25, fusing only two-band subsets Bsubsets (1 ∪ 15) already provided very good AD results where most anomalies were detected, and the background was sufficiently suppressed. Fusing subsequent band

subsets did not have much impact on their detection results.

To further conduct quantitative analysis, Fig. 26 shows the 3-D ROC curves generated from Fig. 24 along with their three corresponding 2-D ROC curves. Table XII tabulates various AUC values where the best results are boldfaced. Apparently, the best overall performance was produced by $((1 \cup 15) \cup 2) \cup 14$. However, if we only look at AUC values of (D, F) , all values are either 0.9997 or 0.9998 with an error range within 10^{-4} . This shows why using $AUC_{(D,F)}$ alone could not work. As for the best BS, it would be 1 ∪ 15, while $((1 \cup 15) \cup 2) \cup 14$ yielded the best TD.

TABLE XIII
COMPUTING TIMES REQUIRED BY PBSF-MBS AND NO-PBSF

Band subsets	computing time (ms)			
	HYDICE data		AVIRIS data	
	no-PBSF	PBSF-MBS	no-PBSF	PBSF-MBS
B_{VIS}	49.05	36.01	253.63	211.89
B_{NIR}	43.39	35.78	293.74	211.78
B_{SWIR}	49.90	36.38	319.79	213.20
B_{VIS} UB_{NIR}	57.86	37.67	325.59	215.65
B_{VIS} UB_{SWIR}	61.95	37.42	370.25	220.01
B_{NIR} UB_{SWIR}	60.37	37.11	413.86	221.30
B_{VIS} UB_{NIR} UB_{SWIR}	80.52	38.91	460.80	222.81

TABLE XIV
COMPUTING TIMES REQUIRED BY PBSF-UBS AND NO-PBSF FOR HYDICE DATA

Number of band subsets	Computational time (ms)	
	no-PBSF	PBSF-UBS
1	40.03	35.15
2	41.36	35.81
3	41.07	35.51
4	42.37	35.57
5	42.44	35.66
6	48.21	35.82
7	49.88	35.90
8	49.90	36.38
9	52.99	36.34
10	54.12	36.65
11	59.15	36.67
12	58.03	37.32
13	62.09	37.72
14	64.79	37.97
15	68.08	38.03
16	68.48	38.08
17	74.12	38.45
18	80.52	38.91

TABLE XV
COMPUTING TIMES REQUIRED BY PBSF-UBS AND NO-PBSF FOR AVIRIS DATA

Number of band subsets	Computing time (ms)	
	No-PBSF	PBSF-UBS
1	239.98	209.35
2	250.29	212.20
3	260.32	210.63
4	280.80	213.91
5	297.83	214.16
6	310.01	213.18
7	327.18	213.63
8	331.63	214.97
9	349.58	219.04
10	369.56	214.25
11	385.64	217.32
12	413.86	221.30
13	426.85	220.61
14	460.80	222.81

IX. COMPUTATIONAL COMPLEXITY

This section presents a computing time analysis of R-AD with/without PBSF-MBS and PBSF-UBS. All experiments

were run on a computer with Intel Core i7-6700 and 8-GB memory, the OS is Windows 10, and the platform is MATLAB R2018a.

Table XIII shows a comparative analysis of the computing time required by R-AD with PBSF and with no-PBSF for two hyperspectral images where the computing time required by R-AD using PBSF was less than that required by R-AD with no-PBSF when R-AD processed the same band set, and its computing time was not affected by the number of bands in the band set. On the contrary, the computing time required by R-AD with no-PBSF was susceptible to the number of bands to be processed and increased as the number of bands in a band subset was increased.

Tables XIV and XV also tabulate the computing times required by R-AD with PBSF-UBS and with no-PBSF for the HYDICE data and AVIRIS data, respectively.

As we can see from Tables XIV and XV, when the number of band subsets was increased, the computing time required by R-AD with no-PBSF was increased proportionally. However, since PBSF realizes RT capability via fusion taking place in R-AD, its computing time was not affected by the number of band subsets and remained unchanged.

X. CONCLUSION

This article presents a new innovative concept of PBSF for AD from a data communication and transmission perspective. Two specific applications are developed for PBSF. One is PBSF-MBS that fuses MBSs progressively in RT. The other is PBSF-UBS that fuses bands uniformly selected by different initial bands. A key concept of PBSF is its fusion actually taking place in an AD but not AD maps. As a consequence, PBSF can be implemented in RT progressively during data acquisition. This is quite different from BS that is considered a postprocessing technique with full data needed to be acquired in advance. It is also different from data fusion that fuses data and sensor fusion that fuses different types of sensors. Several significant results of this article can be summarized as follows.

- 1) PBSF can work exactly the same as SBF when it fuses one single band with a band subset.
- 2) The progressive fusion of MBS is completely new and has never been explored in the past.
- 3) Progressive fusion of band subsets by UBS using different initial bands is also new.
- 4) The fusion equations derived from (4) to (7) are applicable to any operator, which utilizes the sample covariance/correlation matrix to take care of spectral correlation. An immediate application is target detection, such as CEM.
- 5) It has potential advantages for future developments of hyperspectral data communication, specifically, satellite or UAV data communication and transmission.

APPENDIX

(A1), as shown at the top of the next page, where $v_{B_{s,m}B_{t,n}|B_{s,m}} = R_{B_{s,m}}^{-1} X_{B_{s,m}} X_{B_{t,n}}$ and $\beta_{B_{s,m}B_{t,n}|B_{s,m}} = (X_{B_{t,n}}^T [P_{\perp}^T] X_{B_{s,m}}^T)^{-1}$.

$$\begin{aligned}
\delta_{B_{s,m}B_{t,n}}^{\text{RAD}} &= \mathbf{r}_{B_{s,m}B_{t,n}}^T \mathbf{R}_{B_{s,m}B_{t,n}}^{-1} \mathbf{r}_{B_{s,m}B_{t,n}} \\
&= \left(\mathbf{r}_{B_{s,m}}^T, \mathbf{r}_{B_{t,n}}^T \right) \begin{bmatrix} \mathbf{R}_{B_{s,m}}^{-1} + \frac{1}{N} v_{B_{s,m}B_{t,n}|B_{s,m}} \beta_{B_{s,m}B_{t,n}|B_{s,m}} v_{B_{s,m}B_{t,n}|B_{s,m}}^T & -v_{B_{s,m}B_{t,n}|B_{s,m}} \beta_{B_{s,m}B_{t,n}|B_{s,m}} \\ -\beta_{B_{s,m}B_{t,n}|B_{s,m}} v_{B_{s,m}B_{t,n}|B_{s,m}}^T & N\beta_{B_{s,m}B_{t,n}|B_{s,m}} \end{bmatrix} \begin{pmatrix} \mathbf{r}_{B_{s,m}} \\ \mathbf{r}_{B_{t,n}} \end{pmatrix} \\
&= \mathbf{r}_{B_{s,m}}^T \mathbf{R}_{B_{s,m}}^{-1} \mathbf{r}_{B_{s,m}} + \frac{1}{N} \mathbf{r}_{B_{s,m}}^T v_{B_{s,m}B_{t,n}|B_{s,m}} \beta_{B_{s,m}B_{t,n}|B_{s,m}} v_{B_{s,m}B_{t,n}|B_{s,m}}^T \mathbf{r}_{B_{s,m}} - \mathbf{r}_{B_{t,n}}^T \beta_{B_{s,m}B_{t,n}|B_{s,m}} v_{B_{s,m}B_{t,n}|B_{s,m}}^T \mathbf{r}_{B_{s,m}} \\
&\quad - \mathbf{r}_{B_{s,m}}^T v_{B_{s,m}B_{t,n}|B_{s,m}} \beta_{B_{s,m}B_{t,n}|B_{s,m}} \mathbf{r}_{B_{t,n}} + N \mathbf{r}_{B_{t,n}}^T \beta_{B_{s,m}B_{t,n}|B_{s,m}} \mathbf{r}_{B_{t,n}} \\
&= \delta_{B_{s,m}}^{\text{R-AD}} + \frac{1}{N} \left(\mathbf{r}_{B_{s,m}}^T v_{B_{s,m}B_{t,n}|B_{s,m}} - N \mathbf{r}_{B_{t,n}}^T \right) \beta_{B_{s,m}B_{t,n}|B_{s,m}} \times \left(v_{B_{s,m}B_{t,n}|B_{s,m}}^T \mathbf{r}_{B_{s,m}} - N \mathbf{r}_{B_{t,n}} \right) \tag{A1}
\end{aligned}$$

REFERENCES

- [1] W. Sun and Q. Du, "Hyperspectral band selection," *IEEE Geosci. Remote Sens. Mag.*, vol. 7, no. 2, pp. 118–139, Jun. 2021.
- [2] R. N. Patro, S. Subudhi, P. K. Biswal, and F. Dell'Acqua, "A review of unsupervised band selection techniques," *IEEE Geosci. Remote Sens. Mag.*, vol. 9, no. 3, pp. 72–111, Sep. 2021.
- [3] P. Pudil, J. Novovičová, and J. Kittler, "Floating search methods in feature selection," *Pattern Recognit. Lett.*, vol. 15, no. 11, pp. 1119–1125, Nov. 1994.
- [4] M. Song, F. Li, C. Yu, and C.-I Chang, "Sequential band fusion for hyperspectral anomaly detection," *IEEE Trans. Geosci. Remote Sens.*, vol. 60, pp. 1–16, 2022.
- [5] C.-I Chang, Q. Du, T.-L. Sun, and M. L. G. Althouse, "A joint band prioritization and band-decorrelation approach to band selection for hyperspectral image classification," *IEEE Trans. Geosci. Remote Sens.*, vol. 37, no. 6, pp. 2631–2641, Nov. 1999.
- [6] H. Yang, Q. Du, H. Su, and Y. Sheng, "An efficient method for supervised hyperspectral band selection," *IEEE Geosci. Remote Sens. Lett.*, vol. 8, no. 1, pp. 138–142, Jan. 2011.
- [7] Y. Wang, L. Wang, H. Xie, and C.-I Chang, "Fusion of various band selection methods for hyperspectral imagery," *Remote Sens.*, vol. 11, no. 18, p. 2125, Sep. 2019, doi: [10.3390/rs11182125](https://doi.org/10.3390/rs11182125).
- [8] Y. Wang *et al.*, "Constrained-target band selection for multiple-target detection," *IEEE Trans. Geosci. Remote Sens.*, vol. 57, no. 8, pp. 6079–6103, Aug. 2019.
- [9] X. Shang *et al.*, "Target-constrained interference-minimized band selection for hyperspectral target detection," *IEEE Trans. Geosci. Remote Sens.*, vol. 59, no. 7, pp. 6044–6064, Jul. 2021.
- [10] C.-I Chang, *Real-Time Progressive Hyperspectral Image Processing: Endmember Finding and Anomaly Detection*. New York, NY, USA: Springer, 2016.
- [11] C.-I Chang, *Real-Time Recursive Hyperspectral Sample and Band Processing: Algorithm Architecture and Implementation*. New York, NY, USA: Springer, 2017.
- [12] C.-I Chang, L. C. Lee, B. Xue, M. Song, and J. Chen, "Channel capacity approach to band subset selection for hyperspectral imagery," *IEEE J. Sel. Topics Appl. Earth Observ. Remote Sens.*, vol. 10, no. 10, pp. 4630–4644, Oct. 2017.
- [13] L. Wang *et al.*, "Band subset selection for anomaly detection in hyperspectral imagery," *IEEE Trans. Geosci. Remote Sens.*, vol. 55, no. 9, pp. 1–12, Jun. 2017.
- [14] L. Wang, H.-C. Li, B. Xue, and C.-I Chang, "Constrained band subset selection for hyperspectral imagery," *IEEE Geosci. Remote Sens. Lett.*, vol. 14, no. 11, pp. 2032–2036, Nov. 2017.
- [15] C. Yu, M. Song, and C.-I Chang, "Band subset selection for hyperspectral image classification," *Remote Sens.*, vol. 10, no. 1, p. 113, Jan. 2018, doi: [10.3390/rs10010113](https://doi.org/10.3390/rs10010113).
- [16] Q. Wang, Q. Li, and X. Li, "Hyperspectral band selection via adaptive subspace partition strategy," *IEEE J. Sel. Topics Appl. Earth Observ. Remote Sens.*, vol. 12, no. 12, pp. 4840–4950, Dec. 2019.
- [17] Q. Wang, Q. Li, and X. Li, "A fast neighborhood grouping method for hyperspectral band selection," *IEEE Trans. Geosci. Remote Sens.*, vol. 59, no. 7, pp. 608–619, Jul. 2020.
- [18] Q. Wang, F. Zhang, and X. Li, "Optimal clustering framework for hyperspectral band selection," *IEEE Trans. Geosci. Remote Sens.*, vol. 56, no. 10, pp. 5910–5922, Oct. 2018.
- [19] I. S. Reed and X. Yu, "Adaptive multiple-band CFAR detection of an optical pattern with unknown spectral distribution," *IEEE Trans. Acoust., Speech Signal Process.*, vol. 38, no. 10, pp. 1760–1770, Oct. 1990.
- [20] C.-I Chang and S.-S. Chiang, "Anomaly detection and classification for hyperspectral imagery," *IEEE Trans. Geosci. Remote Sens.*, vol. 40, no. 6, pp. 1314–1325, Jun. 2002.
- [21] C.-I Chang, "Hyperspectral anomaly detection: A dual theory of hyperspectral target detection," *IEEE Trans. Geosci. Remote Sens.*, vol. 60, pp. 1–20, 2022.
- [22] C.-I Chang, "Constrained energy minimization anomaly detection for hyperspectral imagery via dummy variable trick," *IEEE Trans. Geosci. Remote Sens.*, vol. 60, pp. 1–19, 2022.
- [23] C.-I Chang, "Hyperspectral target detection: Hypothesis testing, signal-to-noise ratio, and spectral angle theories," *IEEE Trans. Geosci. Remote Sens.*, vol. 60, pp. 1–23, 2022.
- [24] E. J. Candès and M. B. Wakin, "An introduction to compressive sampling," *IEEE Signal Process. Mag.*, vol. 25, no. 2, pp. 21–30, Mar. 2008.
- [25] G. Richard Baraniuk, "Compressive sensing," *IEEE Signal Process. Mag.*, vol. 24, no. 4, pp. 116–124, Jul. 2007.
- [26] C.-I Chang, "Band sampling for hyperspectral imaging," *IEEE Trans. Geosci. Remote Sens.*, vol. 60, pp. 1–24, 2022.
- [27] A. Khristov, (Jun. 2022). *Zig-Zag Pattern Used in en:JPEG Entropy Coding*. [Online]. Available: https://en.wikipedia.org/w/index.php?title=Zig-Zag_Pattern_Used_in_en:JPEG_Entropy_Coding&oldid=107441110
- [28] M. Rabbani and P. W. Jones, *Digital Image Compression Techniques*. Bellingham, WA, USA: SPIE, 1991.
- [29] C.-I Chang, "An effective evaluation tool for hyperspectral target detection: 3D receiver operating characteristic curve analysis," *IEEE Trans. Geosci. Remote Sens.*, vol. 59, no. 6, pp. 5131–5153, Jun. 2021.
- [30] N. Otsu, "A threshold selection method from gray-level histograms," *IEEE Trans. Syst., Man, Cybern.*, vol. SMC-9, no. 1, pp. 62–66, Jan. 1979.
- [31] C.-I Chang, *Hyperspectral Imaging: Techniques for Spectral detection and Classification*. Norwell, MA, USA: Kluwer, 2003.
- [32] C.-I Chang and Q. Du, "Estimation of number of spectrally distinct signal sources in hyperspectral imagery," *IEEE Trans. Geosci. Remote Sens.*, vol. 42, no. 3, pp. 608–619, Mar. 2004.
- [33] C.-I Chang, "A review of virtual dimensionality for hyperspectral imagery," *IEEE J. Sel. Topics Appl. Earth Observ. Remote Sens.*, vol. 11, no. 4, pp. 1285–1305, Apr. 2018.
- [34] J. C. Harsanyi, W. Farrand, and C.-I Chang, "Detection of subpixel spectral signatures in hyperspectral image sequences," *Proc. Amer. Congr. Surveying Mapping (ACSM)/Amer. Soc. Photogramm. Remote Sens. (ASPRS), Annu. Conv. Expo.*, Baltimore, MD, USA, vol. 1, 1994, pp. 236–247.
- [35] C.-I Chang and H. Ren, "An experiment-based quantitative and comparative analysis of target detection and image classification algorithms for hyperspectral imagery," *IEEE Trans. Geosci. Remote Sens.*, vol. 38, no. 2, pp. 1044–1063, Mar. 2000.
- [36] C.-I Chang, *Hyperspectral Data Processing: Algorithm Design and Analysis*. Hoboken, NJ, USA: Wiley, 2013.
- [37] X. Kang, X. Zhang, S. Li, K. Li, J. Li, and J. A. Benediktsson, "Hyperspectral anomaly detection with attribute and edge-preserving filters," *IEEE Trans. Geosci. Remote Sens.*, vol. 55, no. 10, pp. 5600–5611, Oct. 2017.
- [38] R. C. Gonzalez and R. E. Woods, *Digital Image Processing*, 4th ed. Upper Saddle River, NJ, USA: Prentice-Hall, 2018.

- [39] C.-I Chang, Y. Du, J. Wang, S.-M. Guo, and P. Thouin, "A survey and comparative study of entropic and relative entropic thresholding techniques," *IEE Proc., Vis., Image Signal Process.*, vol. 153, no. 6, pp. 837–850, Dec. 2006.
- [40] L. Li, W. Li, Q. Du, and R. Tao, "Low-rank and sparse decomposition with mixture of Gaussian for hyperspectral anomaly detection," *IEEE Trans. Cybern.*, vol. 51, no. 9, pp. 4363–4372, Sep. 2021.
- [41] C.-I Chang, "Effective anomaly space for hyperspectral anomaly detection," *IEEE Trans. Geosci. Remote Sens.*, vol. 60, pp. 1–24, 2022.
- [42] S. Sun, J. Liu, X. Chen, W. Li, and H. Li, "Hyperspectral anomaly detection with tensor average rank and piecewise smoothness constraints," *IEEE Trans. Neural Netw. Learn. Syst.*, early access, Mar. 4, 2022, doi: 10.1109/TNNLS.2022.3152252.
- [43] P. Xiang, H. Li, J. Song, D. Wang, J. Zhang, and H. Zhou, "Spectral-spatial complementary decision fusion for hyperspectral anomaly detection," *Remote Sens.*, vol. 14, no. 4, p. 943, Feb. 2022, doi: 10.3390/rs14040943.
- [44] S. Wang, X. Wang, L. Zhang, and Y. Zhong, "Deep low-rank prior for hyperspectral anomaly detection," *IEEE Trans. Geosci. Remote Sens.*, vol. 60, pp. 1–17, 2022.



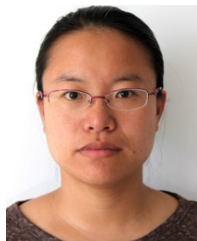
Yulei Wang received the B.S. and Ph.D. degrees in signal and information processing from Harbin Engineering University, Harbin, China, in 2009 and 2015, respectively.

She was awarded by the China Scholarship Council in 2011 as a Joint Ph.D. Student to study at the Remote Sensing Signal and Image Processing Laboratory, University of Maryland at Baltimore County, Baltimore, MD, USA. She is currently an Associate Professor with the College of Information Science and Technology, Dalian Maritime University, Dalian, China. Her research interests include hyperspectral image processing and vital sign signal processing.



Fang Li received the B.E. degree in network engineering from Qufu Normal University, Rizhao, China, in 2017. She is currently pursuing the Ph.D. degree in computer science and technology with Dalian Maritime University, Dalian, China.

Her research interests include hyperspectral imaging, band fusion, and applications.



Meiping Song received the Ph.D. degree from the College of Computer Science and Technology, Harbin Engineering University, Harbin, China, in 2006.

From 2013 to 2014, she was a Visiting Associate Research Scholar with the Remote Sensing Signal and Image Processing Laboratory, University of Maryland at Baltimore County, Baltimore, MD, USA. She has been a Professor with the College of Information Science and Technology, Dalian Maritime University, Dalian, China, since 2006.

2020. Her research interests include remote sensing and hyperspectral image processing.



Chein-I Chang (Life Fellow, IEEE) received the B.S. degree in mathematics from Soochow University, Taipei, Taiwan, in 1973, the M.S. degree in mathematics from the Institute of Mathematics, National Tsing Hua University, Hsinchu, Taiwan, in 1975, the M.A. degree in mathematics from the State University of New York at Stony Brook, Stony Brook, NY, USA, in 1977, the M.S. and M.S.E.E. degrees from the University of Illinois at Urbana-Champaign, Urbana, IL, USA, in 1982, and the Ph.D. degree in electrical engineering from the University of Maryland, College Park, MD, USA, in 1987.

He has been with the University of Maryland at Baltimore County (UMBC), Baltimore, MD, since 1987, where he is currently a Professor with the Department of Computer Science and Electrical Engineering. He has authored four books: *Hyperspectral Imaging: Techniques for Spectral Detection and Classification* (Kluwer Academic Publishers, 2003), *Hyperspectral Data Processing: Algorithm Design and Analysis* (John Wiley & Sons, 2013), *Real-Time Progressive Hyperspectral Image Processing: Endmember Finding and Anomaly Detection* (Springer, 2016), and *Real-Time Recursive Hyperspectral Sample and Band Processing: Algorithm Architecture and Implementation* (Springer, 2017). He also edited three books, *Recent Advances in Hyperspectral Signal and Image Processing* (2006), *Hyperspectral Data Exploitation: Theory and Applications* (John Wiley & Sons, 2007), and *Advances in Hyperspectral Image Processing Techniques* (Wiley, 2022), and co-edited with A. Plaza a book on *High Performance Computing in Remote Sensing* (CRC Press, 2007). His research interests include multispectral/hyperspectral image processing, automatic target recognition, and medical imaging.

Dr. Chang is also a fellow of Society for Photo-optical Instrumentation Engineers (SPIE). He received the National Research Council Senior Research Associateship Award from 2002 to 2003 sponsored by the U.S. Army Soldier and Biological Chemical Command, Edgewood Chemical and Biological Center, Aberdeen Proving Ground, MD. He also serves as an Associate Editor for *Remote Sensing* and *IEEE TRANSACTIONS ON GEOSCIENCE AND REMOTE SENSING*.



Chunyan Yu (Member, IEEE) received the B.Sc. and Ph.D. degrees in environmental engineering from Dalian Maritime University, Dalian, China, in 2004 and 2012, respectively.

In 2004, she joined the College of Computer Science and Technology, Dalian Maritime University. From June 2013 to June 2016, she was a Post-Doctoral Fellow with the Information Science and Technology College, Dalian Maritime University. From September 2014 to September 2015, she was a Visiting Scholar with the College of

Physicians and Surgeons, Columbia University, New York, NY, USA. She has been an Associate Professor with the Information Science and Technology College, Dalian Maritime University, since 2019. Her research interests include image segmentation, hyperspectral image classification, and pattern recognition.